Design of an Analog Adaptive Piezoelectric Sensoriactuator

by

Christopher A. Fannin

Thesis submitted to the Faculty of the

Virginia Polytechnic Institute and State University

in partial fulfillment of the requirements for the degree of

MASTER OF SCIENCE

IN

MECHANICAL ENGINEERING

APPROVED:

William R. Saunders, Chair

Alfred L. Wicks

Harley H. Cudney

February 26, 1997

Blacksburg, VA

Keywords: Piezoelectric, Collocated, Smart Structure, LMS Algorithm, System ID

DESIGN OF AN ANALOG ADAPTIVE PIEZOELECTRIC SENSORIACTUATOR

by

Christopher A. Fannin

Dr. William R. Saunders, Chair

Department of Mechanical Engineering

(ABSTRACT)

In order for a piezoelectric transducer to be used as a sensor and actuator simultaneously, a direct charge due to the applied voltage must be removed from the total response in order to allow observation of the mechanical response alone. Earlier researchers proposed electronic compensators to remove this term by creating a reference signal which destructively interferes with the direct piezoelectric charge output, leaving only the charge related to the mechanical response signal. This research presents alternative analog LMS adaptive filtering methods which accomplish the same result. The main advantage of the proposed analog compensation scheme is its ability to more closely match the order of the adaptive filter to the assumed dynamics of the piezostructure using an adaptive first-order high-pass filter. Theoretical and experimental results are provided along with a discussion of the difficulties encountered in trying to achieve perfect compensation of the feedthrough capacitive charge on a piezoelectric wafer

Acknowledgements

I would like to sincerely thank all of the members of my committee for their help along the course of this research. I would especially like to thank, my advisor, Will Saunders for his encouragement and guidance throughout my Master's program of study. I have enjoyed doing research with him and value the freedom granted me to pursue my graduate studies at my own pace. I would also like to thank Dan Cole for his assistance in various aspects of this research.

I would like to thank all my friends for their companionship and support both scholastically and personally. I'd especially like to thank John Heilmann, a brilliant study partner and trout fishing mentor, Randy Hibshman, loyal ski buddy, fishing pal, and easily one of the nicest people I know, Alexander Hanuska, my roommate and close friend of 4 years. Congratulations and best wishes to Alex and Carol on your marriage.

I would finally like to thank my family. I am glad that we are close; doing things together and never passing up the opportunity to visit and share. I value the relationships that I have with all of you, and I know that we will never grow distant. Congratulations to my sister, Teresa, and brother-in-law, Chris. May your lives be filled with happiness and joy. Finally, thanks to Mom and Dad. You've always given me your love and support and for that I am grateful.

Table of Contents

List of Figures

Nomenclature

A .....gain of adaptive filter

B ..... corner of adaptive filter

C.....damping matrix of a smart structure

d .....desired signal (also V_{01})

e .....error signal (also V_{out})

E .....expected value operator

F..... transfer function of a filter

G .....transfer function of a signal

H .....transfer function of mechanical response

K ..... stiffness matrix of a smart structure

m .....vector of DC offsets on LMS integrators

m_e ..... DC offset on error signal

m_X .....vector of DC offsets on reference signals

M..... mass matrix of a smart structure

P .....cross correlation between desired and input

q_P.....vector of charges on a piezoelectric smart structure

q .....vector of misadjustments in filter weights

r..... generalized coordinate vector

R ..... input correlation matrix

S_{vv} .....spectral density of input voltage

v ..... vector of input voltages to a smart structure

V_{in} .....input voltage signal

V_{out} ..... output voltage signal (same as error signal)

V_{01} .....output of piezostructure circuit (same as desired signal)

V_{02} .....output of adaptive circuit

W_{opt}..... optimal Wiener weights of adaptive filter

X ..... vector of reference signals

y .....output of adaptive circuit (also V_{02})

δ .....time signal of feedthrough electrical term

ρ ..... adaptation parameter

σ^2..... variance of a signal

ω.....circular frequency

ω_r..... mode r natural frequency

ω_1 .....bandwidth of input excitation

ξ_r ..... mode r damping ratio

Θ ..... electromechanical coupling matrix

Θ_r ..... mode r electromechanical coupling

1. Introduction

1.1 Introduction and Objectives

Piezoelectric materials are often used as sensors or actuators in smart structure applications because of their electromechanical coupling characteristics. When a voltage is applied to a piezoelectric material, it will strain. Likewise, a strained piezoelectric will induce a charge which can be measured and used as a sensor response. If strain rate is the desired response, then current is sensed. When the piezoelectric material is used as both as sensor and actuator simultaneously, the sensor response consists of a direct charge term as a result of applying the actuator voltage across the piezoelectric capacitance in addition to the mechanically induced charge. In order to isolate the mechanically induced charge from the dominant capacitance-induced charge, some sort of compensation has to be used. The circuit described in this thesis is a strain rate formulation which will adaptively remove the feedthrough electrical term using all analog circuitry.

Traditionally, the method of removing the direct term has been to combine the piezoelectric charge response with the response of a simple capacitor having a value similar to the capacitance of the piezoelectric material. However, because of the signal-to-noise ratio between the mechanical response and direct response, and uncertainty regarding the exact capacitance of the piezoelectric element, very fine tuning is required for optimal compensation. An adaptive approach would be useful since it would compensate for the discrepancies automatically.

The circuit presented in this thesis is an analog adaptive filter which compensates the output of an active high-pass filter containing the electrical and mechanical dynamics of a piezoelectric element. This approach follows the work of Vipperman and Clark (1995) who presented a similar approach, but with a digital adaptive algorithm. The analog adaptive filter can be realized completely with the use of operational amplifiers and multipliers on a circuit board, and requires no additional equipment such as analog-to-digital converters and digital signal processing hardware to function.

The author wishes to demonstrate the validity of this technique for system identification and control of adaptive structures by meeting the following objectives:

- Demonstrate that the adaptive filter will theoretically converge to match the electrical feedthrough dynamics of the piezoelectric circuit.
- Discuss and quantify sources of error in the adaptation.
- Measure collocated response using the adaptive Sensoriactuator circuit and compare with a model and nearly collocated beam response.
- Use the circuit for collocated rate feedback control.

1.2 Motivation

Because of their sensing and actuation capabilities, piezoelectric materials have received considerable attention in adaptive structure applications in recent years. In particular, piezoceramics have the actuation authority desired for structural and acoustic control. They have also been proposed as a means for doing experimental modal analysis,

since there is direct coupling of the piezoelectric charge components and the structural mode shapes.

For modal analysis and rate feedback control applications, a collocated input/output response is generally desired. In experimental modal analysis this is called a drive point response and facilitates proper scaling of residue terms. The original purpose of this Sensoriactuator investigation was to measure collocated response for system identification purposes. Experimental modal testing was then to be used in an adaptive structure non-dimensional scaling analysis. The idea had already been shown theoretically and a conference paper resulted which clearly demonstrated the application of non-dimensional scaling to adaptive structures and included model results. Experimental results were to follow with modal testing of several different configurations. These experiments were to include both geometrically similar and dissimilar adaptive structures to corroborate theoretical developments which predicted that scaling analyses could be performed with structures that weren't geometrically similar, provided the dissimilarity was relatively minor.

However, attempts to replicate previous formulations of the Sensoriactuator proved difficult, and in an attempt to improve the response, the complexity of the compensation technique continually increased. Attention was soon turned away from the scaling analyses to development of a wholly analog adaptive compensation technique for collocated response measurement.

1.3 Summary of Findings

The investigation revealed that existing compensation techniques did not provide enough flexibility in matching the reference leg response to the dynamics of the direct term, which prompted development of a more flexible, two-weight, adaptive circuit. To demonstrate the merits of the new technique over the old, two circuits were constructed employing analog LMS adaptive techniques. The first of these was a single-weight filter, similar to the one constructed by Vipperman and Clark, featuring a reference leg whose gain was set adaptively. The second circuit used an adaptive high-pass filter to compensate the first-order feedthrough dynamics and added the flexibility of both adaptive magnitude and corner frequency.

Experiments were run to demonstrate and compare the performance of each circuit realization. These included gradual and abrupt changes in piezoelectric capacitance to test system robustness, forcing at a variety of input voltage levels to evaluate the effects on adaptation, and imposing DC offsets into the circuits to investigate robustness of the designs in the face of unwanted signals. The results of these tests were provided in the form of experimental frequency response functions (FRFs). The metric of comparison was a numerical model of the beam, as well as an experimentally derived, nearly-collocated beam response.

The adaptation of the two-weight circuit was accurate provided the excitation voltage was as high as allowable, minimizing the harmful effects of DC offsets in the circuit, which cause the adaptive weights to converge improperly. The sensitivity of the

circuit to DC offset error was observed both by changing the input voltage level, and by introducing intentional offsets into the system and is probably the biggest problem with the design. The user must be cognizant of this condition and take care to minimize unwanted DC offsets especially from the analog LMS integrators.

The two-weight filter adaptation was found to be very robust with regards to both gradual and abrupt changes in piezoelectric capacitance. The system underwent a one second transient adaptation after which it converged once again to the desired solution, leaving only the mechanical strain rate response in the output. The single-weight circuit was unable to successfully adapt to any variations in the piezoelectric capacitance because of its comparatively inflexible design which excluded variability in the first-order corner frequency of the reference leg. The capability of the two-weight compensator to adaptively change the corner frequency of its adaptive high-pass filter is a clear advantage for Sensoriactuator performance.

1.4 Presentation of Thesis

Following this introduction, there will be a discussion of some of the relevant background material pertaining to this design. There is a brief discussion of how piezoelectric materials can be used for system identification and control of adaptive structures, and why a collocated Sensoriactuator response is desirable. Following that is a synopsis of the state-of-the-art in Sensoriactuator design and contributions from various investigators to the designs and methodologies. Because this particular design features an

analog realization of the well-known LMS algorithm, some words will follow on its formulation and implementation.

Chapter 3 describes the previous adaptive Sensoriactuator design and then proceeds to build on it and detail the final design of the adaptive two-weight filter featured in this research. Every attempt is made to clarify and explain each detail of the design and present it in a logical fashion to the reader. The analog LMS realization is posed and described in detail. Additionally, analyses are presented for the convergence of the adaptive algorithm, showing that it will render the desired response. Finally, the issue of DC offset error is addressed and it is clearly shown that the error varies inversely with the input correlation matrix, implying that maximizing input voltage will minimize offset error.

All of the details of the experiments are described in Chapter 4. First, the setup and procedure are described, followed by experimental FRFs of single and two-weight adaptive realizations of the Sensoriactuator. The results presented in this section clearly demonstrate the advantages of the two-weight circuit over the other techniques.

The final chapter will conclude and discuss the future work, which will most immediately consist of refining the design for use in active rate feedback control applications. The results shown in this thesis represent excitation voltages below 1 volt, which is adequate for an experimental modal test, but falls far short of what is required for structural vibration control authority. The challenge is to excite the structure with high voltages, while protecting the Sensoriactuator circuitry. Initial tests have been performed with a high voltage version, with promising results. However, further development is required.

2. Literature Review

2.1 Adaptive Structures: History and Uses

Piezoelectric smart structures have received a considerable amount of attention in recent years because of their versatility and adaptability in difficult-to-model applications such as space trusses. Such a structure can contain hundreds of embedded or surface mounted piezoelectric elements which provide both sensing and actuation capability, allowing for a number of flexible control strategies, such as continuous, hierarchical, or wave control algorithms, which cannot be achieved with a small number of conventional sensors and actuators (Crawley and deLuis, 1987).

The basic premise that a distributed network of sensors and actuators on a structure provides a more effective means of control of both flexural as well as rigid body modes has spawned research into many areas of intelligent structure applications for piezoelectric materials. In the aerospace community, for example, use of piezoelectrics has been investigated for use as integrated actuators for helicopter rotor blade control (Spangler and Hall, 1990), in the suppression of supersonic panel flutter in aircraft or re-entry vehicles (Scott and Weissaar, 1994), and for static control of aeroelastic stiffness of wings (Ehlers and Weissaar, 1993) to name a few. Their relatively small size make them ideally suited for retrofits of existing structures, provided a means exists for properly attaching them.

In order to successfully design fixed gain controllers for any type of smart structure, it is necessary to have an accurate system model. In the case of structures, one easy way to obtain an accurate model is with an experimental modal test. Several authors have written on the coupled effects of piezoelectric elements and structural dynamics, including those previously mentioned.

Hagood *et. al.* (1990) presented coupled piezoelectric-structural dynamic relations allowing for the accurate modeling of smart structures with stiffness and mass loading from piezoelectric sensors and actuators. The analysis presented a general electroelastic model derived using a Rayleigh-Ritz variational formulation. The resulting two main equations are shown below and relate the electrical and mechanical dynamics of any smart structure.

$$M\ddot{r} + C\dot{r} + Kr = \Theta v \tag{2.1}$$

$$\Theta^T r + C_P v = q_P \tag{2.2}$$

In these equations, r is the generalized mechanical coordinate vector, v is the vector of applied voltages, q_P is the vector of electrode charges, Θ is the electromechanical coupling matrix, and C_P is the matrix of piezoelectric capacitances. The equations describe the dynamics of a smart structure with the traditional forcing function being replaced with an electrically induced strain actuator, and the response being a function of the mechanical strain and applied voltage (if any) on the sensor.

These two dynamic relations not only facilitate the development of accurate dynamic models of smart structures, but also form the theoretical basis for determining the

input-output relationships for separate elements in adaptive structures. This implies that the network of piezoelectric sensors and actuators in a smart structure can be used in performing an experimental modal analysis. Saunders *et. al.* (1994) demonstrated that piezostructures were ideally suited for modal parameter estimation. Cole *et. al.* (1995) extends this discussion to include calculation of drive point response using excitation patches as collocated Sensoriactuators.

2.2 The Sensoriactuator: Advent and Development

A Sensoriactuator refers to a piezoelectric element used as a sensor and actuator simultaneously. Because the actuator part necessitates applying a voltage to induce strain, by Equation 2.2 above, it is obvious that a piezoceramic used in this manner contains two terms in the sensor output: the mechanical response term, $\Theta^T r$, which is the response of the beam to piezoelectric excitation and the feedthrough charge term caused by the voltage applied across the piezoelectric capacitance, $C_P v$. Because the piezoelectric is used as both sensor and actuator simultaneously, the arrangement is collocated, which is a useful property from a system ID standpoint.

Several investigators have looked into the problem of collocated sensing and actuation. Dosch *et. al.* (1992) and Anderson *et. al.* (1992) demonstrated a method for compensation of the electrical term in a strain rate configuration, where strain rate is proportional to current. The basic premise is to match the electrical part of the collocated response with the response of a parallel circuit containing a reference capacitor that is equal to the piezoelectric capacitance. Then, subtracting the output of the reference

circuit from the piezoelectric circuit response, the electrical part is canceled, leaving only the mechanical response of the structure. A simple circuit diagram of the strain rate compensation scheme is shown.

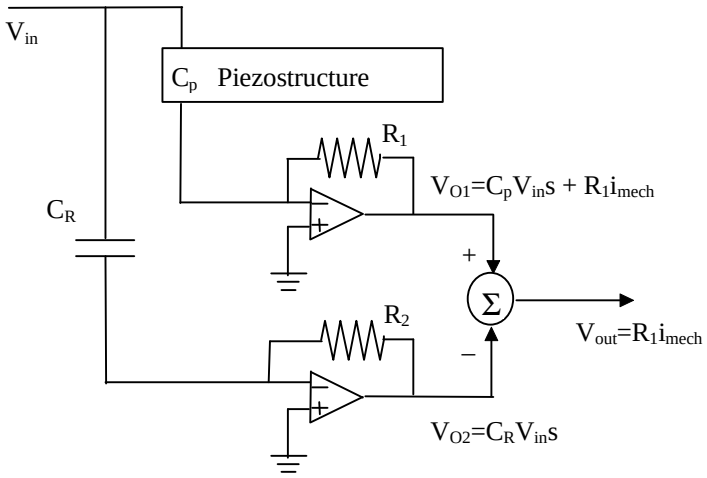

Figure 2.1 - Strain rate analog compensation scheme (differentiating op-amps)

Using this type of configuration, both Dosch *et. al.* and Anderson *et. al.* demonstrated the effectiveness of piezoelectric "self-sensing actuators" and "sensorators" for collocated rate feedback control applications. They also discussed some of the difficulties and limitations of the compensation scheme. For example, Anderson said that "Day-to-day changes in capacitance values proved significant enough to require readjustment of the circuit." It proved very difficult to identically match the piezoelectric capacitance with a reference capacitor, and the degraded performance of the compensator was attributed to differences between the circuit components and variations with time and temperature. Hysteretic nonlinearities were also cited as contributors. Despite using

seemingly identical piezoelectric wafers as reference capacitors to account for temperature variations, the compensator required continual readjustment.

Spangler and Hall (1994) used the same compensation scheme for broadband active damping of a space truss using a collocated piezoelectric strut, but included all of the electrical circuit dynamics in their control plant transfer functions. Making assumptions about the relative importance of the active strut as a sensor or actuator based on the stiffness of the strut and structure, they were able to select a reference capacitor and reference amplifier gain setting to meet their needs without worrying about identically compensating out the electrical response term.

Later, in light of the variations that lead to circuit misadjustment, Cole and Clark (1994) proposed an adaptive approach to the Sensoriactuator problem. Acknowledging that piezoceramics exhibit nonlinear variations in their piezoelectric constants as a function of applied voltage and temperature, an adaptive digital compensation technique was proposed to track the unsteady capacitance. Using a charge-compensating configuration, they showed that the optimal Wiener solution for a single-weight, adaptive filter used to numerically approximate the patch capacitance, was indeed equal to the patch capacitance assuming the inputs to the system had a uniform (white) spectral distribution. Thus, it was theoretically proven that a digital filter could optimally track the piezoelectric capacitance.

Following on that work, Vipperman and Clark (1995) invented a hybrid analog and digital adaptive compensator. The circuitry was a strain rate realization. It used a reference capacitor which was close to the actual piezoelectric capacitance, and then an analog multiplier, tuned by a digital signal processor (DSP) to adaptively scale the

reference circuit magnitude. They demonstrated the convergence assuming white inputs, and presented experimental and theoretical frequency response functions. This compensator proved to be an effective means to adaptively match the electrical feedthrough sensor dynamics.

The compensator was demonstrated in a collocated rate feedback beam vibration controller using a low level white noise training signal for the adaptation. It was asserted that the adaptive filter would only remove components of the circuit output coherent to the input, making it effective for disturbance rejection.

2.3 Analog LMS: Theory and Implementation

Vipperman and Clark used the well-known least mean squares (LMS) adaptive algorithm as presented by Widrow and Stearns (1985). This algorithm, using a steepest descent on an error performance surface, finds the filter coefficient that minimizes the error signal variance. Because they posed the "error" signal as the compensator output (the sum of V_{01} and V_{02}), when the error variance was minimized, the direct electrical term was removed and the mechanical response remained.

The work that is to be presented in this thesis closely follows on the work of Vipperman and Clark, but identifies a wholly analog method for achieving the Sensoriactuator adaptively. Because the compensation method makes use of a single-weight finite impulse response (FIR) filter, an analog realization is quite straight forward. It consists of an LMS block for each filter weight (in this case one), which is built using an

analog multiplier and integrator. This analog LMS approach was presented as long ago as 1967 by Widrow*et. al.*

More recently, Karni and Zeng re-derived the analog LMS algorithm using a bilinear transformation of the digital algorithm and found the optimal Wiener solution using instantaneous, unbiased estimates of the input correlation matrix and the cross correlation vector of input to desired signals. They demonstrated that, unlike the discrete filter, the analog is theoretically stable for any adaptive gain (the analog equivalent of step size). In practice, the stability is limited by non-ideal behavior of electronics and DC voltages on various components. The analog weight update equation is shown.

$$\frac{d}{dt}W(t) = \rho e(t)X(t) \tag{2.3}$$

In Equation 2.3, W(t) is the adaptive filter weight, e(t) is the error signal being minimized by the LMS algorithm, and X(t) is the reference input to the adaptive filter. It is easy to see that when both sides are integrated, the adaptive filter weight can be generated as shown in Figure 2.2. A variation on this form is the steepest descent algorithm, which replaces the reference input with a gradient signal (like the one used by Vipperman and Clark).

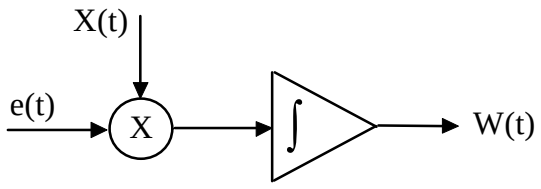

Figure 2.2 - Block diagram of analog LMS block

Several papers have been written on the design of analog adaptive filters. Most of these center around the implementation with regards to minimizing adaptation error due to DC offsets in the adaptive circuitry and/or LMS adaptation algorithm. Shoval *et. al.* (1995) showed that the excess mean squared error due to DC offsets in the circuitry varies inversely with the input signal power. In other words, as input power increases, the error in adaptive filter weights decreases, improving the adaptive filter performance. The DC offset error is shown to be affected by the input signal power through the input correlation matrix, R. This same reference asserts that offsets in the LMS integrators typically dominate the error terms, stressing the importance of using properly null adjusted integrating op-amps in the adaptive circuitry.

The following chapter explains the design of the two-weight compensator by first describing the adaptive scheme presented by Vipperman and Clark, and then building on that design. The choice and implementation of circuit hardware is presented and discussed. Finally, the analog LMS algorithm is derived for use with the proposed design and analyzed for optimal performance and sensitivity to DC offset errors.

3. Analog Adaptive Sensoriactuator

3.1 Hybrid Digital/Analog Compensation

The circuit designed by Vipperman and Clark used an analog multiplier with a digital, single-weight FIR filter implemented with a DSP chip to scale the reference circuit output for effective cancellation of the electrical part of the sensor response. A circuit diagram of the hybrid system appears in Figure 3.1 below.

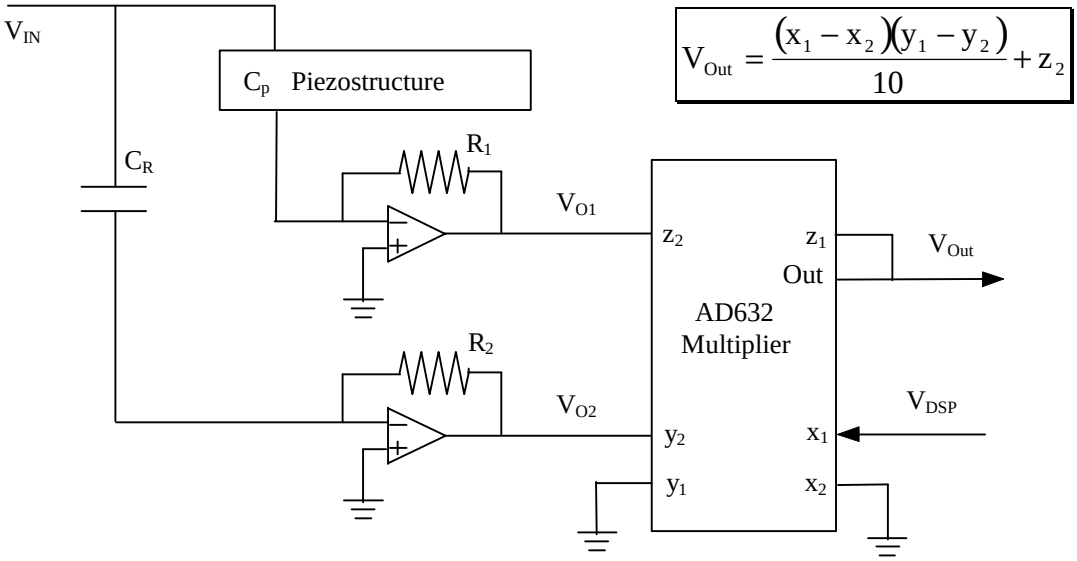

Figure 3.1 - Sensoriactuator compensation circuit by Vipperman and Clark (1995)

The adaptive circuit uses two operational amplifiers in a differentiating configuration; a piezoceramic transducer made of Lead Zirconate Titanate (PZT) is connected to one amplifier and a reference capacitor is connected to the other. When the output of the reference circuit is properly scaled by an adaptive LMS algorithm, the electrical feedthrough component is canceled leaving mechanical strain rate information only in $V_{Out.}$

In addition to the two differentiating op amps, the circuit requires an AD632 analog multiplier chip and a DSP chip running a single-weight LMS adaptive algorithm. The voltage output of the piezostructure circuit, V_{O1}, and the reference capacitor circuit, V_{O2}, are both fed into the multiplier where V_{O2} is multiplied by V_{DSP} and added to V_{O1}. The voltage output of the LMS algorithm, V_{DSP} , is used to scale the output voltage of the reference circuit so that the output of the multiplier, V_{Out}, is minimized. Assuming that the phase of the electrical part of V_{O1} and the phase of V_{O2} are 180° apart, the minimized output of the AD632 will contain only mechanical strain rate response information.

Casting this circuit in an adaptive signal processing light, the output of the compensation system, $V_{Out}(k)$, can be considered the error signal, e(k); the output of the PZT circuit, $V_{01}(k)$, is the desired signal, d(k); the output of the multiplier, $V_{02}(k)*V_{DSP}/10$, is the adaptation circuit output, y(k). The digital part of the hybrid system is the well-known LMS algorithm. A single-weight FIR filter is implemented on a DSP board to adjust the gain on the compensating voltage, V_{O2}. From Figure 3.1 above, it is easily shown that the output voltage is defined as follows:

$$V_{Out}(t) = \frac{V_{DSP}\left(-R_2 C_R \frac{dV_{IN}}{dt}\right)}{10} - R_1 C_P \frac{dV_{IN}}{dt} - R_1 \frac{\partial q_{mech}}{\partial t} \tag{3.1}$$

where q_{mech} is simply the part of Equation 2.2 that contains the mechanical response of the piezostructure. The instantaneous power in the output signal, given by the cost function in Equation 3.2, can be minimized using a steepest descent method. This is the basis of the adaptive LMS algorithm.

$$J = E[V_{Out}^2] \tag{3.2}$$

It can be shown that the LMS weight update equation yields an expression for the adaptive compensating signal V_{DSP} as the weight update as shown below. The gradient term can be found by differentiating the adaptation circuit output with respect to the weight, V_{DSP}.

$$V_{DSP} \approx w(k) + \mu 2 V_{Out}(k) \frac{V_{O2}(k)}{10} \tag{3.3}$$

The result in Equation 3.3 is exactly that which is presented by Vipperman and Clark (1995) and demonstrates a clever marriage of digital and analog circuitry for compensation of the feedthrough capacitance in a Sensoriactuator. The weight update is performed on a DSP and is used to scale an analog circuit output using an analog multiplier.

3.1.1 Practical Implementations and Limitations

The circuitry described above relies heavily on the reference capacitor being similar to the piezoelectric capacitance in the primary leg of the circuit. The reason for this is the relative phase between the two circuits. Should the phase response not match perfectly (to within 1 degree at every frequency), the system will be unable to cancel out the electrical feedthrough response of the Sensoriactuator. This phase matching is critical because of the relative magnitudes of the mechanical and electrical parts of the total Sensoriactuator response. The mechanical response is often observed to be more than 25dB lower in magnitude than the electrical part. Because of variations in circuit components, piezoelectric capacitance, and poor circuit design methods, the relative phases of the two legs of the circuit will seldom turn out to be 180° from one another without meticulous adjustment of the reference capacitance.

This sensitivity can be demonstrated using two high-pass filters; one in the reference leg of the adaptive circuit, the other in place of the piezoelectric differentiator. They are constructed using similar resistors and capacitors, one having a potentiometer on the input to allow for adjustment of the corner frequency. There is no mechanical response term, so the output should be at the electronic noise floor when the two filters' outputs are added together with 0 phase difference. Figure 3.2 shows an uncompensated first-order response, a compensated response which is just above the noise floor and a compensated response with a 2 degree phase error (brought about by changing the corner frequency potentiometer) between the two legs of the circuit. This shows that the total

possible reduction is limited by the amount of phase mismatch between the two legs of the circuit.

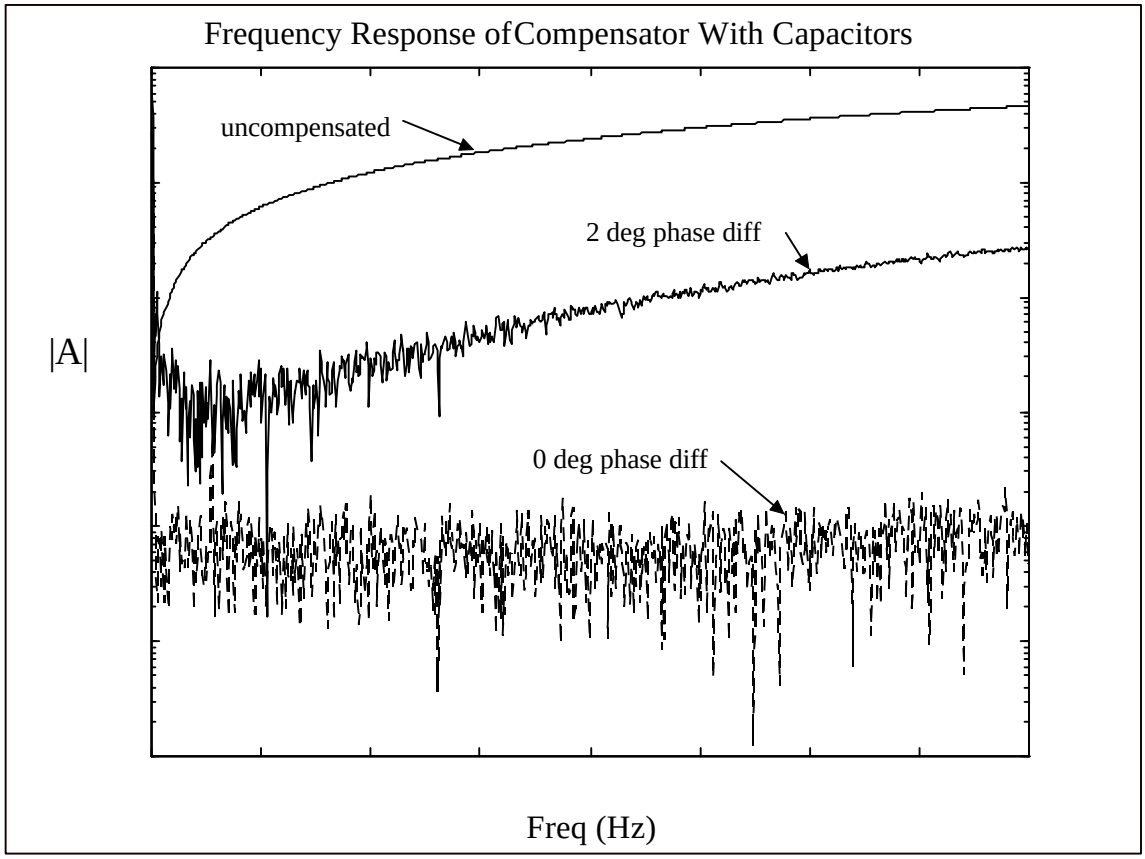

Figure 3.2 - Sensitivity to phase error between the two legs of the compensator

3.2 Improved Differentiator Circuitry

Using op-amps in a pure differentiating realization amplifies noise, tends easily toward saturation, and is undesirable from a closed loop stability standpoint. Franco

(1988) discusses the detrimental effects (i.e. reduced phase margin in the closed loop op-amp configuration) caused by the ideal differentiator curve crossing the op-amp's open loop gain curve. The result is a high Q resonant peak at the gain crossover frequency, with the high frequency closed loop response trailing off along the open loop gain curve of the op-amp.

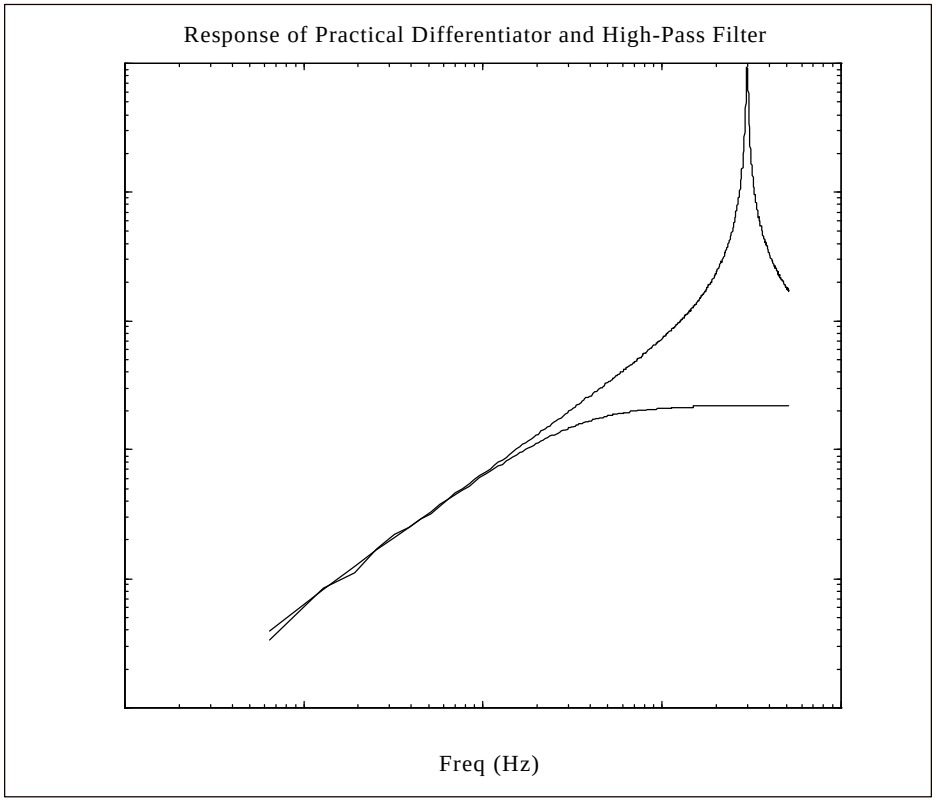

Figure 3.3 - A practical differentiator with large resonant peak at the gain crossover frequency.

The amplification of high frequency noise and potential for oscillation is evident in Figure 3.3 which shows a measured frequency response of a differentiator along with a high-pass filter response. It is common practice to alleviate the troubles associated with differentiating op-amps by adding a resistor to form a high-pass filter which acts like a differentiator in a user prescribed bandwidth. It is evident that the two responses shown are almost identical at frequencies below 1000 Hz.

A comparison of the simple modification to the reference circuit described by Vipperman and Clark (1995) is shown in Figure 3.4. The figure shows the two configurations along with Bode magnitude plots of the ideal amplifier responses. The amplifier in Figure 3.4(a) is subject to higher-order dynamics and noise in the viscinity of the gain crossover frequency. Because of the high frequency amplification, saturation is also a problem for practical differentiators, thereby limiting the voltage input amplitude. These problems are alleviated by adding a pole at f_c. The circuit in Figure 3.4(b) acts like a differentiator between f_o and f_c, but has more phase margin in the closed loop configuration and is therefore a more stable circuit. In summary, a simple differentiator will not behave ideally at higher frequencies. Despite the fact that this non-ideal behavior occurs at very high frequencies compared to the operating range of interest for the Sensoriactuator, phase discrepancies associated with the differentiating op-amp's second-order response manifest themselves in the Sensoriactuator bandwidth, thereby reducing the ability of a compensating circuit to effectively cancel the capacitance-induced charge (or current) on the piezoelectric. The achievable accuracy using the differentiating, compensating circuit described earlier is dependent on the relative phase of the outputs,

V_{O1} and V_{O2}. Small differences in capacitance between C_P and C_R will result in phase errors because of the non-ideal differentiating op-amps which do not exhibit a 90^o phase response at all frequencies because of the high frequency resonant peak shown previously.

An added benefit to the addition of the first-order pole is the ability to "tune" the relative phases of the PZT and reference circuits. This is easily accomplished by making R_c in the reference circuit a potentiometer. By adjusting R_c, the pole moves slightly, which results in a small shift in phase in the frequency range of interest. Now, rather than relying on the exact matching of the piezoelectric capacitance with a reference capacitor, it is possible to get good phase matching with a tuning potentiometer.

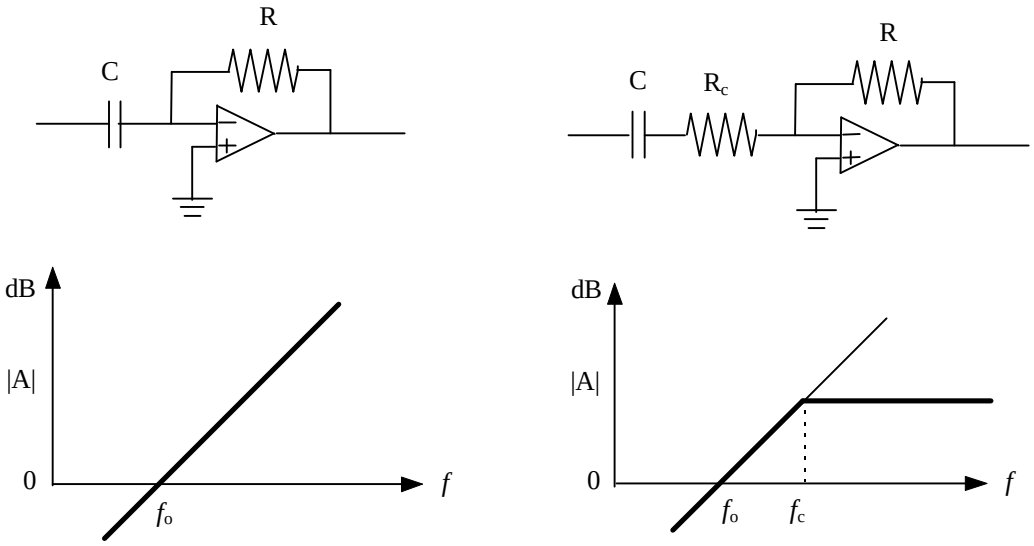

$$f_o = \frac{1}{2\pi RC}$$

(a)

$$f_o = \frac{1}{2\pi RC}, \quad f_c = \frac{1}{2\pi R_c C}$$

(b)

Figure 3.4 - (a) Differentiating amplifier subject to noise and high order dynamic effects (b) Improved differentiator. The corner frequency, f_c, is determined by R_c.

3.3 Single-Weight Analog Compensator

Using the improved differentiator in the same type of configuration that was presented by Vipperman and Clark, and a single-weight analog realization of the LMS algorithm, a new compensation scheme is realized. This new compensator isn't plagued with the same problems of phase mismatch as the former, since the high-pass filter arrangement allows for tuning of the corner frequency, which amounts to tuning the relative phase of the two legs of the compensating circuitry. This means that it isn't as important to match a reference capacitor as with the pure differentiating scheme proposed previously. Additionally, a DSP is no longer required to adaptively compensate the feedthrough capacitance, because an analog LMS is constructed for that task. A full circuit diagram appears in Figure 3.5.

3.3.1 Analog LMS Algorithm

The LMS algorithm used for this realization is identical to the single-weight FIR described by Vipperman and Clark, except that it's built using an analog multiplier and integrator rather than a DSP. The adaptive filter terminology is expressed as follows. The error signal being minimized is considered to be the system output. Once the filter is adapted and the sum of V_{01} and V_{02} minimized, the mechanical response is all that remains. The output of the piezoelectric circuit, V_{01}, is considered to be the desired signal, and the output of the reference leg of the system, V_{02}, is equivalent to the gradient of the output with respect to the FIR weight, V_{adapt} as shown in Equation 3.4.

$$\frac{\partial V_{Out}}{\partial V_{adapt}} = \frac{\partial\left[\frac{V_{adapt}V_{02}}{10} - V_{01}\right]}{\partial V_{adapt}} = \frac{V_{02}}{10} \tag{3.4}$$

3.3.2 Tuning the Compensator

The circuit in Figure 3.5 shows the use of two potentiometers. The first of these is used to tune the corner frequency of the reference circuit relative to the piezoelectric circuit. (This replaces the process of matching a reference capacitor). The second potentiometer is used to adjust the null offset on the LMS integrator. Recall that DC offsets in the LMS integrators cause bias error in the calculation of the adaptive filter weight. Therefore, an algorithm with a null adjusted LMS integrator will converge to a proper scaling voltage, V_{adapt}, barring any other DC voltage sources on that integrator.

The manual tuning procedure for the reference circuit corner frequency is not a simple process. It consists of taking frequency response measurements of both legs of the compensator, comparing the relative phase response within the frequency range of interest (0 -800Hz), adjusting the input potentiometer (changing the corner frequency), and repeating the frequency response measurement and comparison until the relative phase between the two legs is as close to 180° as can practically be achieved. This procedure is quite straight forward for the case of regular capacitors in each leg of the compensator, but when a PZT is inserted, it is very difficult to determine the exact match. After all, some of the phase in this configuration will be coming from mechanical response of the

piezostructure. Of course, it is not desirable to cancel the mechanical response, so it is difficult to know when the circuit is properly tuned.

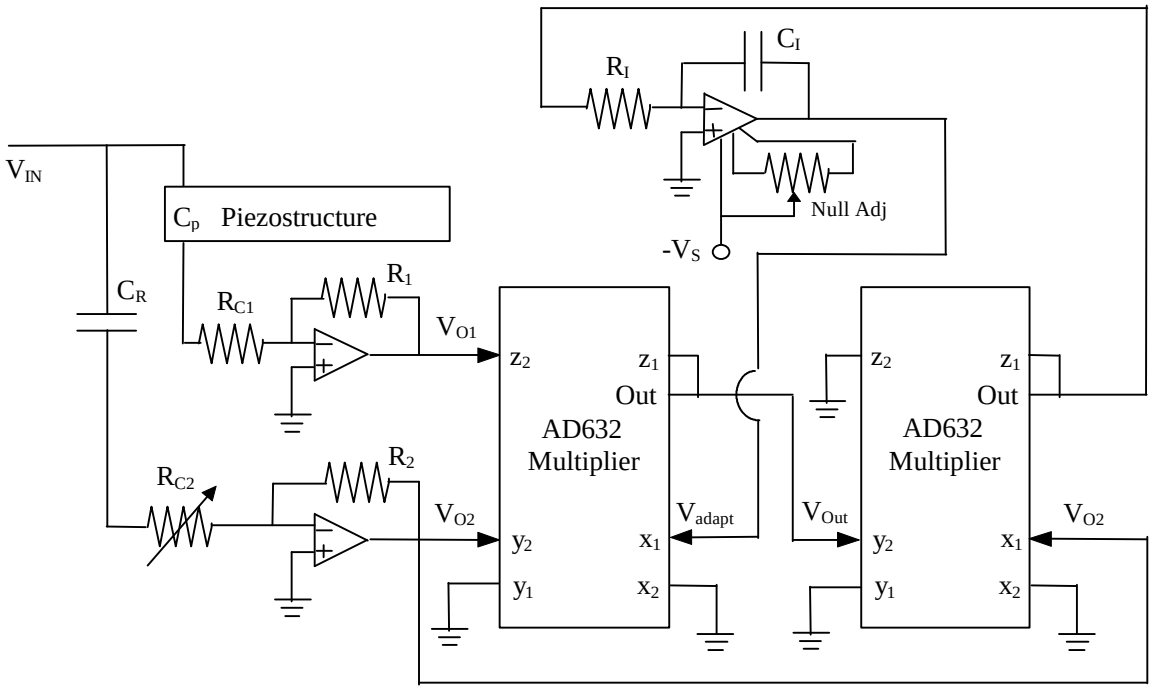

Figure 3.5 - Single-weight analog adaptive compensator

Tuning the LMS null adjust is quite simple. Ideally, the desire is to eliminate any DC component in the op-amp that would cause erroneous adaptation. However, if there are sources of DC offset other than the integrating op-amp, the null adjust can be used to cancel those offsets with an intentional offset on the op-amp. Once the corner frequency has been set as described above, the way to set the null adjust is to simply change it until the output response magnitude is minimized because as Vipperman and Clark showed, a

minimized error corresponds to the output containing only mechanical strain rate information.

This procedure amounts to little more than the required tuning that plagued all previous investigators of the Sensoriactuator problem. Once this tuning is complete, successive adjustments will be performed adaptively by the LMS compensator, thereby making this a seemingly more self-sustaining technique. However, as C_P changes, so does the corner frequency of the feedthrough dynamic response. This affects the relative phase between the piezoelectric and reference legs which results in less accurate compensation. Clearly, what is needed is a means of adapting the corner frequency automatically.

3.4 Two-weight Analog Compensator

Despite the apparent advantages of the analog adaptive approach described above, there are drawbacks that manifest themselves. For example, the nature of the tuning procedure makes the system less robust and more difficult to predict theoretically. Additionally, the first-order dynamics are sensitive to changes in C_P which compromises the integrity of the approach. A two-weight adaptive system, where the corner frequency adaptively changes was sought to add reliability in that it would be more hands-off for the user. In this case, a reference leg had to be built to match the assumed first-order dynamics of the feedthrough electrical term.

3.4.1 First-order Adaptive Filter Design

In order to realize an adaptive high-pass filter, it was necessary to figure out a way to adjust gain and corner frequency using adaptation voltages which would serve as the

weights. The adjustable gain was already in place with the use of the analog multiplier. However, the corner frequency was being manually adjusted with a potentiometer on the single-weight circuit. How could it be to enable an additional weight of adaptation?

The solution was to redesign the high-pass filter of the reference leg altogether. The result is a state filter with two adjustable gain blocks. These two blocks represent the high-pass filter gain and corner frequency. They are realized using voltage controlled amplifiers (VCAs), which change gain based on a command voltage input. Thus, the two-weight LMS can adaptively change the gain and corner of the filter using the LMS block output voltages (the weights) as the command voltages to the VCAs.

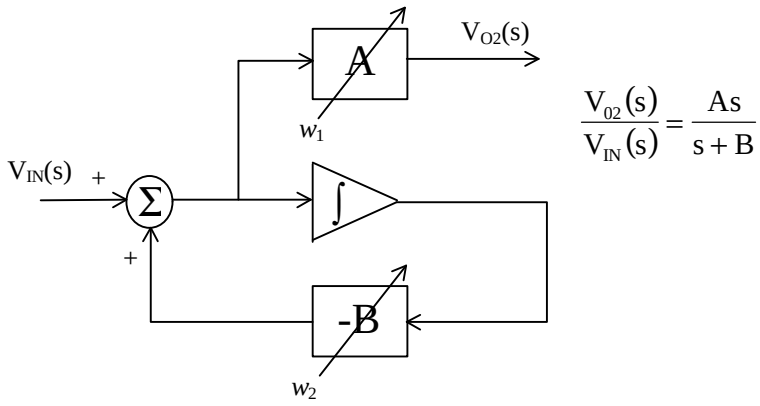

Figure 3.6 - Adaptive high-pass filter block diagram and transfer function

3.4.2 Design for Linear Operation

The adaptive gain blocks were built using Analog Devices SSM2164P voltage controlled amplifiers. These amplifiers have an operating range of -100 dB to 20 dB of gain for command voltages between 3.3 V and -0.6 V, with unity gain for a command

voltage of 0.0 V. There are four VCAs on each 16-pin dual in-line package (DIP), with the closest gain matching between respective amplifiers occurring at unity gain. This feature is important to the design of the LMS algorithm as will become apparent later.

The adaptive high-pass circuit shown in Figure 3.6 was built using inverting VCAs for gain blocks A and B, an inverting summing op-amp, and an inverting integrating op-amp. Because the SSM2164P nominally uses current amplifier configurations, it had to be wired differently for voltage amplification. The circuit diagram below shows the VCA connections for voltage amplification, and results in a 20 dB shift of the dynamic range so that a command voltage of 0.0 V results in a 20 dB voltage gain through the amplifiers.

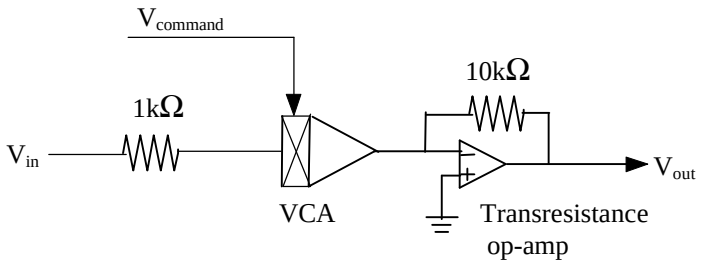

Figure 3.7 - SSM2164P voltage controlled amp configured for voltage amplification.

Because the performance of the adaptive filter depends on the performance of all individual components, every attempt is made to minimize nonlinearities in each VCA. The adaptive amplifier is designed in such a way as to allow the VCAs to adapt to approximately unity gain based on the nominal characteristics of the PZT and corresponding base leg circuitry. This design approach ensures that the VCAs operate in

their linear range, as saturation and other nonlinear problems occur at higher (or lower) gain values. The input power, too, affected the linearity of the VCAs operation, so every attempt was made to keep the input to each VCA low enough to prevent signal distortion due to saturation.

The piezoelectric circuit leg of the compensator is shown in Figure 3.8. The approximate capacitance of the piezoelectric wafers is approximately 30 nF. Looking at the circuit, therefore, it is easily shown that the gain is equal to 15 and the corner is equal to about 15150 based on nominal resistor and capacitor values. In order for the VCAs to operate nominally around 0 dB gain, the remaining op amps in the adaptive high-pass filter are designed so that the nominal transfer function would equal that of the piezoelectric circuit leg when 0.0 V command voltages were applied to the VCAs.

$$\frac{V_{01}(s)}{V_{IN}(s)} = \frac{\frac{R}{R_C}}{s + \frac{1}{C_P R_C}}$$

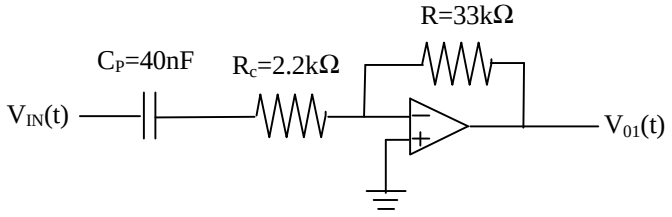

Figure 3.8 - Piezoelectric circuit leg of compensator network

Designing for unity gain operation of the VCAs is quite simple. Because the output of the adaptive high-pass filter, V_{02}, is added to the output of the piezoelectric base leg high-pass filter, V_{01}, the output of either circuit can be scaled by a constant value depending on the input resistors to the summing op-amp. In this case, since the nominal

gain of the piezoelectric base leg circuit is 15, the summer is constructed to amplify the adaptive filter by a factor of 15, allowing the adaptive filter gain block A (see Figure 3.6) to adapt to a nominal gain value of unity.

The integrator of the adaptive filter is constructed using an inverting op-amp. Depending on the values of the resistor and capacitor in that circuit, the gain of the integrator can be adjusted to account for most of the gain that is required in the feedback loop (to properly set the corner frequency with block B). The integrator gain is set to approximately 2595 using an 8200 Ω resistor and 0.047 μF capacitor. Thus, the adaptive filter gain block B (see Figure 3.6) can adapt to a nominal value around 15 dB.

3.4.3 Analog LMS Algorithm

In order to properly configure the adaptive circuitry, the analog LMS realization is posed in a similar manner as before. The output of the compensator is the "error" signal being minimized by the LMS algorithm. This realization can lead to confusion, since the mechanical response is really what is desired. However, in order for the adaptation to work properly, the "desired" signal is posed here as the output of the piezoelectric base leg. This makes sense, since the adaptive circuit is attempting to match the first-order dynamics of the base leg circuit. A block diagram of this adaptive realization appears in Figure 3.9.

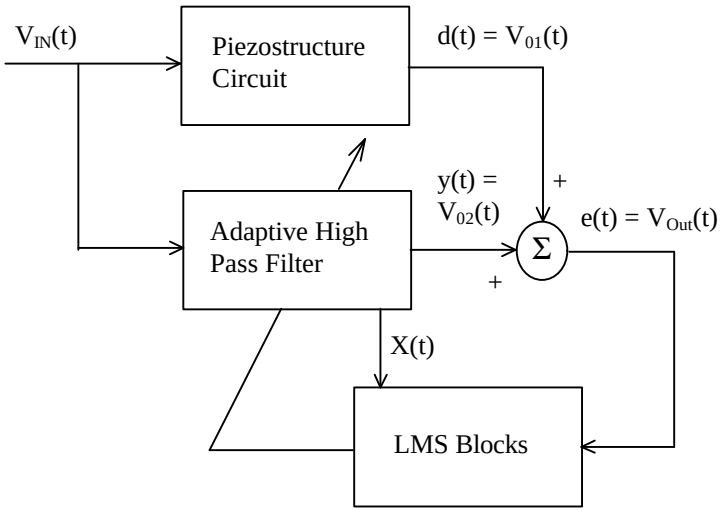

Figure 3.9 - Adaptation block diagram

In addition to the previously mentioned adaptation system components, there are also reference inputs to the LMS blocks. These are derived by looking at the transfer function of the adaptive high-pass filter. First, a simplifying assumption is made. Because the gains A and B of the adaptive filter are proportional to the actual weights of the adaptive LMS blocks, denoted by w_1 and w_2 in Figure 3.6, the weights will be assumed to be equivalent to A and B for subsequent derivations.

Looking at the adaptive filter in Figure 3.6, it is easily seen that the output of the filter is as follows:

$$V_{02}(s) = A\left(V_{IN}(s) - B\frac{1}{s+B} V_{IN}(s) \right) \tag{3.5}$$

Thus, in keeping with our adaptive approach, this equation needs to be re-written in an appropriate form for the adaptive filter output to be a vector multiplication of the weights and reference inputs (see section 3.4.4 for source of reference inputs).

$$y(s) = V_{02}(s) = \sum w_n X_n = AX_1(s) + BX_2(s) \tag{3.6}$$

where

$$X_1(s) = V_{IN}(s) \tag{3.7}$$

$$X_2(s) = -\frac{A}{s+B} V_{IN}(s) \tag{3.8}$$

What remains is to feed the reference inputs to the LMS blocks to allow for adaptation of the high-pass filter. Recall that the adaptive weights are equal to the integral of the product of the error and reference signals.

$$\frac{d}{dt} W_N(t) = \rho e(t) X_N(t) \tag{2.3}$$

Equation 2.3 describes the analog LMS block operation for determining the adaptive filter weights, that in this case are proportional to the gains A and B of the adaptive filter. The first of the two reference inputs is simply the adaptation system input, $V_{IN}(s)$. However, the second reference input is not a signal that is readily available anywhere in the adaptive circuit as it presently stands. Therefore, a means of creating the second reference input had to be devised.

3.4.4 Creating Reference Signal and Circuit Tuning

Looking at the individual signals in the adaptive circuit, the output of the integrator contains all of the needed information for X_2 except for the gain, A. Thus, the reference input can be created by gaining the integrator signal by a value of A. This was accomplished using another VCA in the circuit, one whose gain is equal to and is controlled by the same command voltage as block A, so that a twin A block is formed.

This block is then connected to the integrator's output and, by virtue of it being an inverting amplifier, corrects the sign for the analog LMS. Because the gain matching is best between amplifiers at unity gain, the circuit is designed to allow nominal operation of the A block VCAs at 0 dB. Figure 3.10 shows this realization of the adaptive circuit and reference input, $X_2(t)$.

Now that all of the components of the adaptive system are identified, it is time to present the final outcome. Figure 3.11 shows a system diagram similar to Figure 3.9, but containing more detailed information of the various components. A full circuit diagram is shown in Figure 3.12 illustrating all of the system components.

Tuning of this circuit is very simple. The LMS integrators must be null adjusted to ensure that they are not producing DC offsets that affect the filter convergence. The null adjustment procedure consists of connecting the integrator input to ground, and adjusting the null adjust potentiometer until the integrator output is neither increasing nor decreasing. This procedure should be repeated (or at least verified) at the beginning of each usage of the circuit. This circuit works very well for small excitation voltages where the PZT is operating in a linear range. A circuit that allows for higher voltage excitation signals (such as those necessary for active structural control) is left for future work.

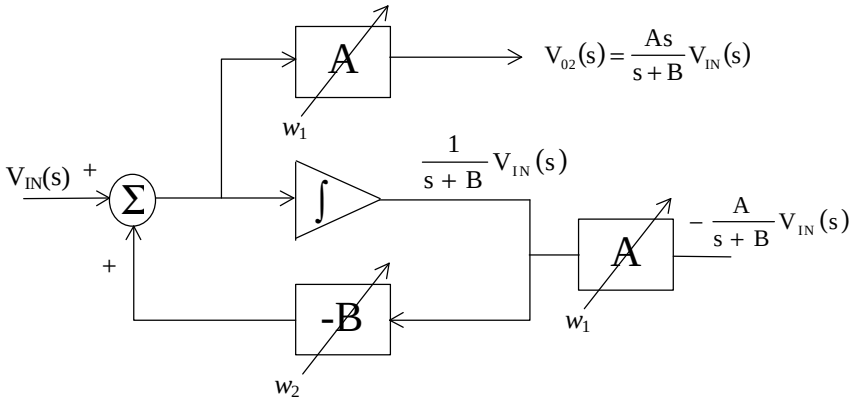

Figure 3.10 - Adaptive circuit with reference input realization X_2

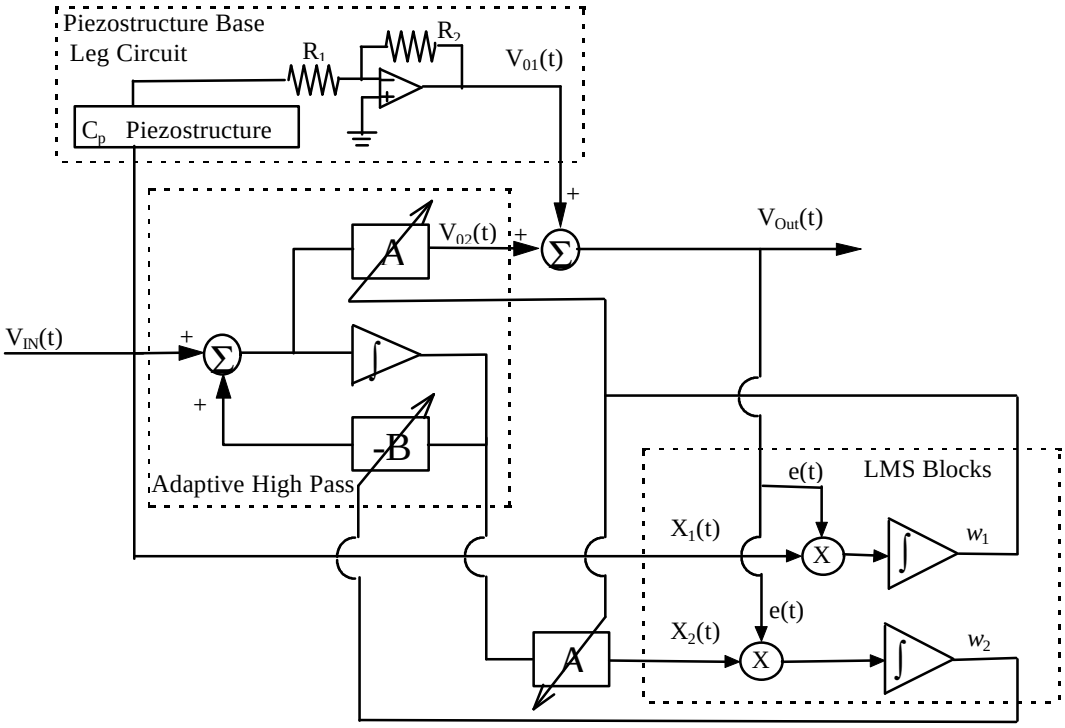

Figure 3.11 - Adaptation system diagram

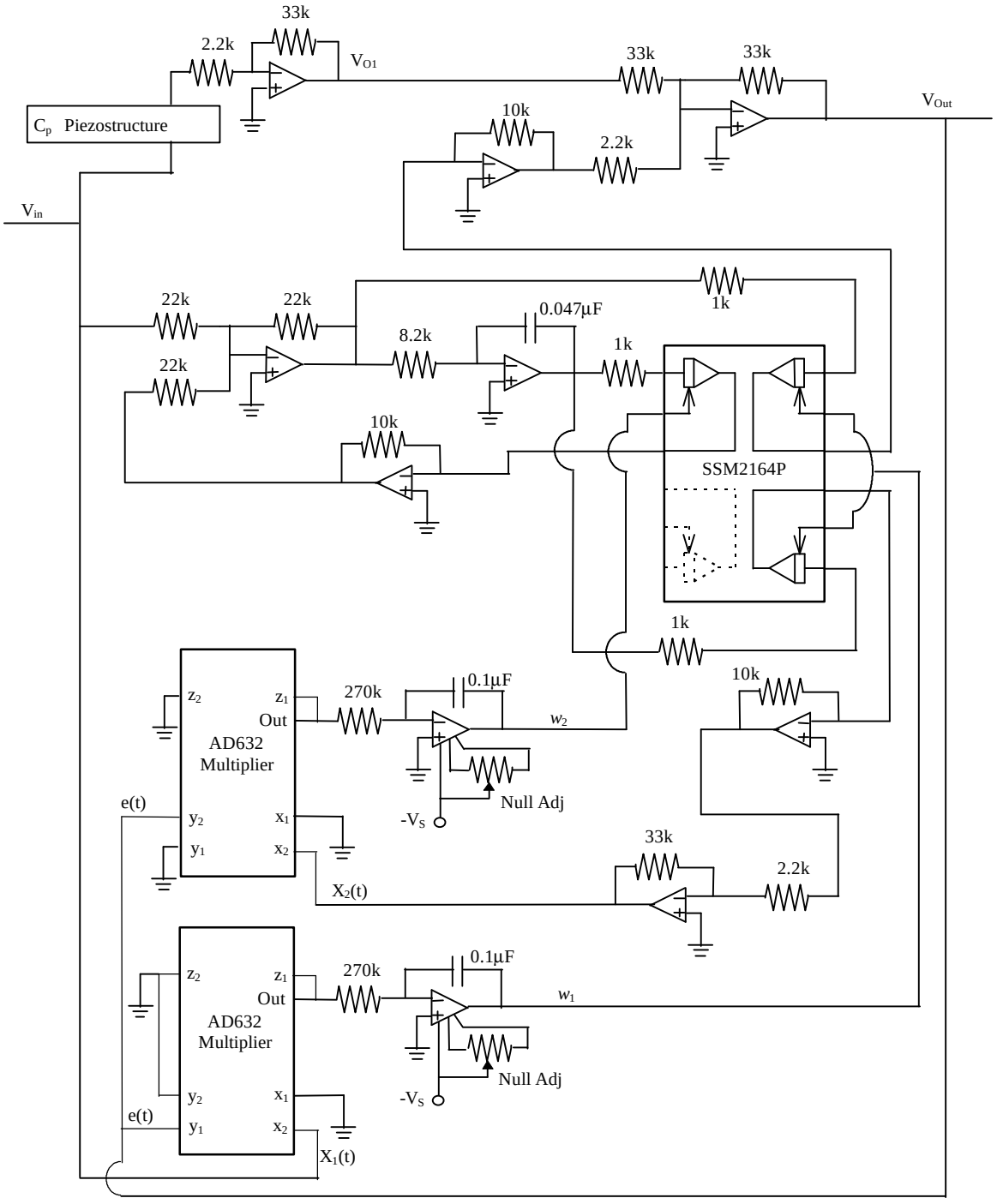

Figure 3.12 - Full circuit diagram of analog adaptation system

3.5 Proof of Adaptive Filter Convergence

Because the LMS algorithm is used, the error (in this case V_{OUT}) will be minimized using the adaptive filter weights. Because this is not an FIR arrangement, however, the performance surface of the adaptation is not guaranteed to have a single, global minimum. Therefore, the first task is to demonstrate a unique solution for minimization of the error signal variance. To do this, the expected value of the error squared, $E[e^2(t)]$, must be found and shown to be minimized when the adaptive filter corner matches the base leg filter corner and likewise, the adaptive filter gain matches the base leg gain.

Assuming for a moment, that the piezoelectric wafer is replaced with an ordinary capacitor (thereby eliminating the mechanical response dynamics), it can be shown that the variance of the error can be driven to zero. The expression for the error signal in the Laplace domain is as follows:

$$e(s) = \left[\frac{As}{s+B} - \frac{\frac{R_2}{R_1}s}{s+\frac{1}{CR_1}} \right] V_{in}(s) = G(s)V_{in}(s) \tag{3.9}$$

The variance of the error is expressed as the expected value of the error squared, which is equal to the integral of the filter output spectral density squared:

$$E\left[e^2(t)\right] = \int_{-\infty}^{\infty} |G(\omega)|^2 S_{VV}(\omega) d\omega \tag{3.10}$$

Assuming the input voltage is white noise with variance σ_v^2 and a bandwidth of $2\omega_1$, evaluating the integral in Equation 3.10 renders the following expression:

$$\sigma_e^2 = -\int_{-\omega_1}^{\omega_1} \left\{ \frac{\left(A - \frac{R_2}{R_1}\right)\omega^2 + \left(B\frac{R_2}{R_1} - A\frac{1}{CR_1}\right)j\omega}{\left(B\frac{1}{CR_1} - \omega^2\right) + \left(B + \frac{1}{CR_1}\right)j\omega} \times \frac{\sigma_v^2}{2\omega_1} \right\} d\omega \qquad (3.11)$$

By inspection of Equation 3.11, it is apparent that the only values that lead to the variance of the error going to zero are as follows:

$$A = \frac{R_2}{R_1} \qquad\qquad B = \frac{1}{CR_1} \qquad (3.12) \text{ \& } (3.13)$$

Thus, the expressions in 3.12 and 3.13 represent a unique solution for the converged LMS filter.

3.5.1 Derivation of Optimal Weights

It has been demonstrated that a unique solution exists that will minimize the error signal of the adaptive filter shown. Now the optimal adaptive filter weights, also known as the Wiener weights, can be found. The Wiener weights are found using the following relation from Widrow and Stearns (1985):

$$W_{opt} = R^{-1}P \qquad (3.14)$$

where R is known as the input correlation matrix and P is the cross correlation vector between the desired response and the input components as defined below. Recall that X(t) is the vector of reference inputs.

$$R(t) = X^T(t)X(t) \qquad (3.15)$$

$$P(t) = V_{01}(t)X(t) \qquad (3.16)$$

These expressions represent instantaneous, unbiased estimates of R and P for this analog realization of the LMS algorithm. Equation 3.14 is valid for an infinite impulse

response (IIR) filter like the one used in the adaptive Sensoriactuator circuit, provided the system has converged and the inputs are stationary (Widrow and Stearns, 1985).

Several assumptions must be made to develop the following proof. First, the filter is assumed to have converged to the unique solution. Therefore, the following substitutions will be made for the filter transfer function coefficients:

$$\hat{A} = A = \frac{R_2}{R_1} \qquad \hat{B} = B = \frac{1}{C_p R_1} \qquad (3.17) \text{ \& } (3.18)$$

The excitation (V_{IN}) is white noise, as before with variance σ_v^2 and a bandwidth of $2\omega_1$, so that the spectral density is as shown:

$$S_{vv}(\omega) = \frac{\sigma_v^2}{2\omega_1} \qquad (3.19)$$

For clarification of notation, the following expressions will be used for the reference inputs. In addition, A and B will be used as equivalent to the adaptive weights for calculation purposes just as they were developed in Equation 3.5.

$$X_1(s) = V_{in}(s) \qquad (3.20)$$

$$X_2(s) = -\frac{\hat{A}}{s + \hat{B}} V_{in}(s) = G(\omega) V_{in}(\omega) \qquad (3.21)$$

To begin, the input correlation matrix will be derived and its inverse calculated. It is a 2 by 2 matrix, since there are two reference inputs.

$$R = E\begin{bmatrix} X_1(t)X_1(t) & X_1(t)X_2(t) \\ X_2(t)X_1(t) & X_2(t)X_2(t) \end{bmatrix} \qquad (3.22)$$

$$R_{11} = \int_{-\infty}^{\infty} V_{in}^*(\omega) V_{in}(\omega) d\omega = \int_{-\omega_1}^{\omega_1} S_{vv}(\omega) d\omega = \sigma_v^2 \qquad (3.23)$$

$$R_{12} = \int_{-\infty}^{\infty} V_{in}^{*}(\omega) G(\omega) V_{in}(\omega) d\omega = \frac{-\hat{A}\sigma_v^2}{2\omega_1} \int_{-\omega_1}^{\omega_1} \frac{1}{\hat{B} + j\omega} d\omega$$
$$= \frac{-\hat{A}\sigma_v^2}{2\omega_1 j} \left[\ln(\hat{B} + j\omega) \right]_{-\omega_1}^{\omega_1} = \frac{-\hat{A}\sigma_v^2}{2\omega_1 j} \ln\left(\frac{\hat{B} + j\omega_1}{\hat{B} - j\omega_1} \right) \tag{3.24}$$

$$R_{21} = \int_{-\infty}^{\infty} G^{*}(\omega) V_{in}^{*}(\omega) V_{in}(\omega) d\omega = \frac{-\hat{A}\sigma_v^2}{2\omega_1} \int_{-\omega_1}^{\omega_1} \frac{1}{\hat{B} - j\omega} d\omega$$
$$= \frac{\hat{A}\sigma_v^2}{2\omega_1 j} \left[\ln(\hat{B} - j\omega) \right]_{-\omega_1}^{\omega_1} = \frac{-\hat{A}\sigma_v^2}{2\omega_1 j} \ln\left(\frac{\hat{B} + j\omega_1}{\hat{B} - j\omega_1} \right) \tag{3.25}$$

$$R_{22} = \int_{-\infty}^{\infty} G^{*}(\omega) V_{in}^{*}(\omega) G(\omega) V_{in}(\omega) d\omega = \frac{\hat{A}^2\sigma_v^2}{2\omega_1} \int_{-\omega_1}^{\omega_1} \frac{1}{\hat{B}^2 - (j\omega)^2} d\omega$$
$$= \frac{\hat{A}^2\sigma_v^2}{2\omega_1} \left[\frac{1}{2j\hat{B}} \ln\left(\frac{\hat{B} + j\omega}{\hat{B} - j\omega} \right) \right]_{-\omega_1}^{\omega_1} = \frac{\hat{A}^2\sigma_v^2}{2\omega_1 \hat{B} j} \ln\left(\frac{\hat{B} + j\omega_1}{\hat{B} - j\omega_1} \right) \tag{3.26}$$

Substituting Eqs. 3.23 through 3.26 into Equation 3.22, and inverting the matrix, the following results.

$$R^{-1} = \frac{\begin{bmatrix} \frac{\hat{A}^2\sigma_v^2}{2\omega_1 \hat{B} j} \ln\left(\frac{\hat{B} + j\omega_1}{\hat{B} - j\omega_1} \right) & \frac{\hat{A}\sigma_v^2}{2\omega_1 j} \ln\left(\frac{\hat{B} + j\omega_1}{\hat{B} - j\omega_1} \right) \\ \frac{\hat{A}\sigma_v^2}{2\omega_1 j} \ln\left(\frac{\hat{B} + j\omega_1}{\hat{B} - j\omega_1} \right) & \sigma_v^2 \end{bmatrix}}{\frac{\hat{A}^2\sigma_v^4}{2\omega_1 \hat{B} j} \ln\left(\frac{\hat{B} + j\omega_1}{\hat{B} - j\omega_1} \right) + \frac{\hat{A}^2\sigma_v^4}{4\omega_1^2} \left\{ \ln\left(\frac{\hat{B} + j\omega_1}{\hat{B} - j\omega_1} \right) \right\}^2} \tag{3.27}$$

Now, the vector of cross correlations between desired and input elements, P will be calculated and the product $R^{-1}P$ computed.

$$V_{01} = \left[\frac{\hat{A}s}{s+\hat{B}} + R_2 \sum_{r=1}^{\infty} \frac{\Theta_r^2 s}{s^2 + 2\xi_r \omega_r s + \omega_r^2} \right] V_{in}(s) = \left[F(\omega) + H(\omega) \right] V_{in}(\omega) \tag{3.28}$$

$$P_1 = E\left[V_{01}(t) X_1(t) \right] = \int_{-\infty}^{\infty} F^*(\omega) V_{in}^*(\omega) V_{in}(\omega) d\omega + \int_{-\infty}^{\infty} H^*(\omega) V_{in}^*(\omega) V_{in}(\omega) d\omega \tag{3.29}$$

The cross correlation vector, like the input correlation matrix, is based on an instantaneous estimate. Because the adaptation is based on a strain rate, rather than a strain signal, there is going to be an instantaneous correlation between the structural response and the reference inputs. However, it is hoped that this effect will be small and that the resulting bias on the optimal weights will be negligible.

$$\begin{aligned}
P_1 &= \frac{-\hat{A}\sigma_v^2 j}{2\omega_1} \int_{-\omega_1}^{\omega_1} \frac{\omega}{\hat{B} - j\omega} d\omega + \sum_r \frac{\sigma_v^2}{2\omega_1} \int_{-\omega_1}^{\omega_1} \frac{-R_2 \Theta_r^2 j\omega}{\omega_r^2 - \omega^2 - 2\xi_r \omega_r j\omega} d\omega \\
&= \frac{-\hat{A}\sigma_v^2 j}{2\omega_1} \left[\frac{-\omega}{j} - \hat{B} \ln\left(\hat{B} - j\omega \right) \right]_{-\omega_1}^{\omega_1} \\
&\quad - \sum_r \frac{R_2 \Theta_r^2 \sigma_v^2 j}{2\omega_1} \left[\begin{array}{l} \frac{-j}{2} \ln\left(\omega_r^2 - \omega^2 - 2\xi_r \omega_r j\omega \right) \\ + \frac{\xi_r}{2\sqrt{1-\xi_r^2}} \ln\left(\frac{-\omega - \omega_r \sqrt{1-\xi_r^2} - \xi_r \omega_r j}{-\omega + \omega_r \sqrt{1-\xi_r^2} - \xi_r \omega_r j} \right) \end{array} \right]_{-\omega_1}^{\omega_1} \\
&= \frac{-\hat{A}\sigma_v^2 j}{2\omega_1} \left[\frac{-2\omega_1}{j} + \hat{B} \ln\left(\frac{\hat{B} - j\omega_1}{\hat{B} + j\omega_1} \right) \right] \\
&\quad - \sum_r \frac{R_2 \Theta_r^2 \sigma_v^2 j}{2\omega_1} \left[\begin{array}{l} \frac{j}{2} \ln\left(\frac{\omega_r^2 - \omega_1^2 + 2\xi_r \omega_r \omega_1 j}{\omega_r^2 - \omega_1^2 - 2\xi_r \omega_r \omega_1 j} \right) \\ + \frac{\xi_r}{2\sqrt{1-\xi_r^2}} \ln\left(\frac{\omega_1^2 + \omega_r^2 \sqrt{1-\xi_r^2} + \xi_r^2 \omega_r^2 + 2\omega_r \omega_1 \sqrt{1-\xi_r^2}}{\omega_1^2 + \omega_r^2 \sqrt{1-\xi_r^2} + \xi_r^2 \omega_r^2 - 2\omega_r \omega_1 \sqrt{1-\xi_r^2}} \right) \end{array} \right]
\end{aligned} \tag{3.30}$$

$$P_2 = E\left[V_{01}(t)X_2(t)\right] = \int_{-\infty}^{\infty} F^*(\omega)V_{in}^*(\omega)G(\omega)V_{in}(\omega)d\omega + \sum_r \int_{-\infty}^{\infty} H^*(\omega)V_{in}^*(\omega)G(\omega)V_{in}(\omega)d\omega \tag{3.31}$$

$$P_2 = \frac{-\hat{A}^2\sigma_v^2 j}{2\omega_1}\int_{-\omega_1}^{\omega_1}\frac{\omega}{\hat{B}^2+\omega^2}d\omega + \sum_r \frac{\sigma_v^2}{2\omega_1}\int_{-\omega_1}^{\omega_1}\left(\frac{-R_2\Theta_r^2 j\omega}{\omega_r^2-\omega^2-2\xi_r\omega_r j\omega}\right)\left(\frac{-\hat{A}}{\hat{B}+j\omega}\right)d\omega$$

$$= \frac{-\hat{A}^2\sigma_v^2 j}{2\omega_1}\int_{-\omega_1}^{\omega_1}\frac{\omega}{\hat{B}^2+\omega^2}d\omega + \sum_r \frac{\hat{A}R_2\Theta_r^2\sigma_v^2}{2\omega_1}\int_{-\omega_1}^{\omega_1}\left(\frac{\omega}{\left(\omega+\omega_r\sqrt{1-\xi_r^2}+\xi_r\omega j\right)\left(\omega-\omega_r\sqrt{1-\xi_r^2}+\xi_r\omega j\right)\left(\omega-\hat{B}j\right)}\right)d\omega$$

$$= \frac{-\hat{A}^2\sigma_v^2 j}{2\omega_1}\left[\frac{1}{2}\ln\left(\hat{B}^2+\omega^2\right)\right]_{-\omega_1}^{\omega_1}$$

$$+\sum_r \frac{\hat{A}R_2\Theta_r^2\sigma_v^2}{2\omega_1}\left[\begin{array}{l}\dfrac{\hat{B}j\ln\left(\omega-\hat{B}j\right)}{-3j\left(\hat{B}j\right)^2+2\left(2\xi_r\omega_r-\hat{B}\right)\left(\hat{B}j\right)+\omega_r^2 j-2\xi_r\omega_r\hat{B}j} \\ +\dfrac{\left(\omega_r\sqrt{1-\xi_r^2}-\xi_r\omega_r j\right)\ln\left(\omega-\omega_r\sqrt{1-\xi_r^2}+\xi_r\omega_r j\right)}{-3j\left(\omega_r\sqrt{1-\xi_r^2}-\xi_r\omega_r j\right)^2+2\left(2\xi_r\omega_r-\hat{B}\right)\left(\omega_r\sqrt{1-\xi_r^2}-\xi_r\omega_r j\right)+\omega_r^2 j-2\xi_r\omega_r\hat{B}j} \\ +\dfrac{\left(-\omega_r\sqrt{1-\xi_r^2}-\xi_r\omega_r j\right)\ln\left(\omega+\omega_r\sqrt{1-\xi_r^2}+\xi_r\omega_r j\right)}{-3j\left(-\omega_r\sqrt{1-\xi_r^2}-\xi_r\omega_r j\right)^2+2\left(2\xi_r\omega_r-\hat{B}\right)\left(-\omega_r\sqrt{1-\xi_r^2}-\xi_r\omega_r j\right)+\omega_r^2 j-2\xi_r\omega_r\hat{B}j}\end{array}\right]_{-\omega_1}^{\omega_1}$$

$$= \frac{-\hat{A}^2\sigma_v^2 j}{4\omega_1}\ln\left(\frac{\hat{B}^2+\omega_1^2}{\hat{B}^2+\omega_1^2}\right)$$

$$+\sum_r \frac{\hat{A}R_2\Theta_r^2\sigma_v^2}{2\omega_1}\left[\begin{array}{l}\dfrac{\hat{B}}{\hat{B}^2+2\hat{B}\xi_r\omega_r+\omega_r^2}\ln\left(\dfrac{\omega_1-\hat{B}j}{-\omega_1-\hat{B}j}\right) \\ -\dfrac{\left(\omega_r\sqrt{1-\xi_r^2}-\xi_r\omega_r j\right)}{2\left(j\omega_r^2-\xi_r^2\omega_r^2 j+\omega_r\sqrt{1-\xi_r^2}\left(\omega_r\xi_r+\hat{B}\right)\right)}\ln\left(\dfrac{\omega_1-\omega_r\sqrt{1-\xi_r^2}+\xi_r\omega_r j}{-\omega_1-\omega_r\sqrt{1-\xi_r^2}+\xi_r\omega_r j}\right) \\ -\dfrac{\left(-\omega_r\sqrt{1-\xi_r^2}-\xi_r\omega_r j\right)}{2\left(j\omega_r^2-\xi_r^2\omega_r^2 j-\omega_r\sqrt{1-\xi_r^2}\left(\omega_r\xi_r+\hat{B}\right)\right)}\ln\left(\dfrac{\omega_1+\omega_r\sqrt{1-\xi_r^2}+\xi_r\omega_r j}{-\omega_1+\omega_r\sqrt{1-\xi_r^2}+\xi_r\omega_r j}\right)\end{array}\right]$$

(3.32)

Thus, the cross correlation vector shows two parts: a cross correlation due to the electrical part and a biasing term due to the mechanical response dynamics. For simplicity, we shall replace the mechanical response bias terms appearing in Equations 3.30 and 3.32

with MR1 and MR2 for subsequent derivations. Note that these bias terms appear to decrease with increasing excitation bandwidth because of the ω_1 in the denominator. This comes about as a direct result of a decrease in the spectral density with increasing excitation bandwidth,ω_1 (see Equation 3.19).

$$P = \begin{bmatrix} \hat{A}\sigma_v^2 + \dfrac{\hat{A}\hat{B}\sigma_v^2 j}{2\omega_1}\ln\left(\dfrac{\hat{B}+j\omega_1}{\hat{B}-j\omega_1}\right) + MR1 \\ 0 + MR2 \end{bmatrix} \tag{3.33}$$

$$W_{opt} = R^{-1}P = \frac{\begin{bmatrix} \dfrac{\hat{A}^3\sigma_v^4}{2\omega_1\hat{B}j}\ln\left(\dfrac{\hat{B}+j\omega_1}{\hat{B}-j\omega_1}\right) + \dfrac{\hat{A}^3\sigma_v^4}{4\omega_1^{\,2}}\ln^2\left(\dfrac{\hat{B}+j\omega_1}{\hat{B}-j\omega_1}\right) + \dfrac{\hat{A}\sigma_v^2}{2\omega_1 j}\ln\left(\dfrac{\hat{B}+j\omega_1}{\hat{B}-j\omega_1}\right)\left(\dfrac{\hat{A}}{\hat{B}}MR1 + MR2\right) \\ \dfrac{\hat{A}^2\sigma_v^4}{2\omega_1 j}\ln\left(\dfrac{\hat{B}+j\omega_1}{\hat{B}-j\omega_1}\right) + \dfrac{\hat{A}^2\hat{B}\sigma_v^4}{4\omega_1^{\,2}}\ln^2\left(\dfrac{\hat{B}+j\omega_1}{\hat{B}-j\omega_1}\right) + \sigma_v^2\left(\dfrac{\hat{A}\sigma_v^2}{2\omega_1 j}\ln\left(\dfrac{\hat{B}+j\omega_1}{\hat{B}-j\omega_1}\right)MR1 + MR2\right) \end{bmatrix}}{\dfrac{\hat{A}^2\sigma_v^4}{2\omega_1\hat{B}j}\ln\left(\dfrac{\hat{B}+j\omega_1}{\hat{B}-j\omega_1}\right) + \dfrac{\hat{A}^2\sigma_v^4}{4\omega_1^{\,2}}\ln^2\left(\dfrac{\hat{B}+j\omega_1}{\hat{B}-j\omega_1}\right)}$$

$$= \begin{bmatrix} \hat{A} + \dfrac{\dfrac{\hat{A}}{\hat{B}}MR1 + MR2}{\hat{A}\sigma_v^2\left(\dfrac{1}{\hat{B}} + \dfrac{j}{2\omega_1}\ln\left(\dfrac{\hat{B}+j\omega_1}{\hat{B}-j\omega_1}\right)\right)} \\ \hat{B} + \dfrac{\dfrac{\hat{A}\sigma_v^2}{2\omega_1 j}\ln\left(\dfrac{\hat{B}+j\omega_1}{\hat{B}-j\omega_1}\right)MR1 + MR2}{\dfrac{\hat{A}^2\sigma_v^2}{2\omega_1}\ln\left(\dfrac{\hat{B}+j\omega_1}{\hat{B}-j\omega_1}\right)\left(\dfrac{1}{\hat{B}j} + \dfrac{1}{2\omega_1}\ln\left(\dfrac{\hat{B}+j\omega_1}{\hat{B}-j\omega_1}\right)\right)} \end{bmatrix} = \begin{bmatrix} \hat{A} + bias \\ \hat{B} + bias \end{bmatrix} \tag{3.34}$$

Thus, it has been demonstrated that, at convergence, the optimal weights reduce to the values for A and B that were desired to match the adaptive filter dynamics to the piezoelectric circuit dynamics. However, a bias term does exist and must be quantified in order to determine whether it is possible to neglect. Even though the correlation in the mechanical response bias terms is reduced as bandwidth increases, the denominator of the

inverted cross correlation matrix, R, also decreases with increasing bandwidth (see Equation 3.27). Because these effects are on the same order when multiplied together in Equation 3.34, and they don't simply divide out, it is not clear what the effect will be on the biased optimal weights.

In order to quantify the bias terms in Equation 3.34, a Matlab code was written which calculated the biased optimal weights as a function of input bandwidth, ω_1. The code appears in the Appendix and uses modal electromechanical coupling values (Θ from Eq. 2.2) obtained from the same model that will be used for comparison of final results in the following chapter (also included in the Appendix). It is apparent from Figure 3.13 that the white noise excitation of the structure should have as large a bandwidth as possible to minimize the bias in the optimal Wiener weights due to mechanical response correlation.

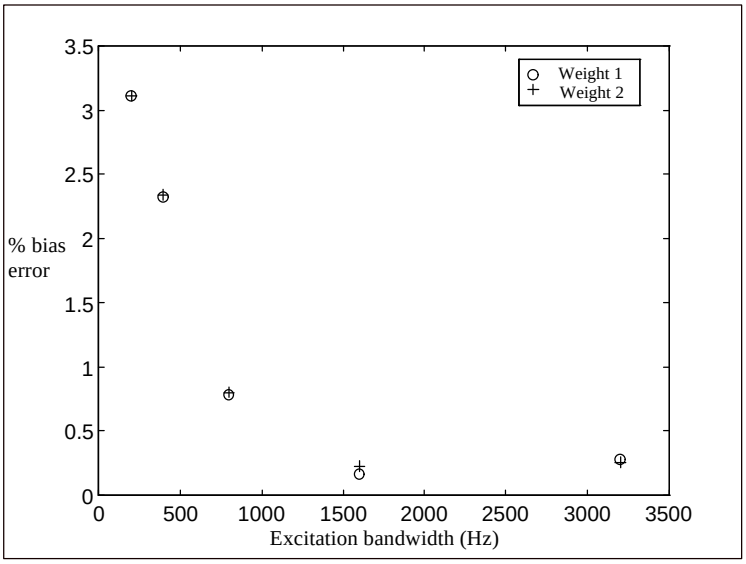

Figure 3.13- Bias error (magnitude) in optimal weights from structural response correlation

As mentioned previously, DC offsets can corrupt the adaptation by biasing the weights, which would also compromise the effectiveness of the Sensoriactuator for providing accurate mechanical response information. The following derivation shows how DC offsets affect the results of the adaptation and how their effects can be minimized.

3.5.2 Effects of DC Offsets on Adaptation Error

When DC voltages appear either in the LMS integrators, the error signal, or on any of the reference signals, the adaptation will be biased. The magnitude of the bias is dependent on the input correlation matrix, as will be shown. In order to demonstrate the effects of DC offsets on the adaptation results, it is necessary to look once again at the weight update equation:

$$\frac{d}{dt}W(t) = \rho e(t)X(t) \tag{2.3}$$

By integrating both sides and assuming there are DC offsets present on the error signal, the reference signals, and the integrator inputs, as shown in Figure 3.14, the following equation results:

$$W(t) = \rho \int_0^t \left[\left(e(\tau) + m_e \right) \left(X(\tau) + m_X \right) + m \right] d\tau \tag{3.35}$$

where m_e is the DC offset in the error signal, m_X is the vector of DC offsets on the reference signals, and m is the vector of DC offsets at inputs of the LMS integrators.

When the algorithm has converged, the weights are constant, therefore the expected value of the term inside the integral of Equation 3.35 is equal to zero.

$$E\left[\left(e(t)+m_e\right)\left(X(t)+m_X\right)+m\right]=0 \tag{3.36}$$

$$E\left[e(t)X(t)+e(t)m_X+m_eX(t)+m_em_X+m\right]=0 \tag{3.37}$$

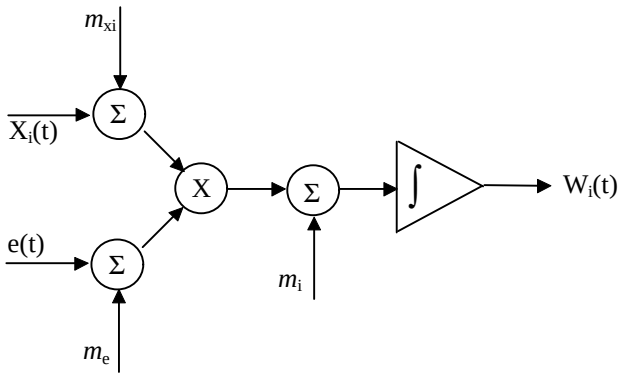

Figure 3.14 - LMS block with DC offsets

The error signal (which once again is the output of the adaptive network) can be expressed as follows:

$$e(t)=\delta(t)+Ri_{mech}-y^*(t)-X^Tq \tag{3.38}$$

where $\delta(t)$ is the electrical part of the desired signal, $y^*(t)$ is the nominal adaptive filter output when fully adapted, and q is the misadjustment in the filter weights due to DC offset errors. When the algorithm converges, $\delta(t)$ and $y^*(t)$ cancel and Equation 3.38 reduces to the mechanical response minus the excess error due to DC offsets.

For zero-mean inputs, $E\left[X(t)\right]=[0]_{2X1}$, and assuming the reference inputs and filter coefficients are statistically independent, they can be separated:

$$E\left[X^T(t)W(t)\right]=E\left[X^T(t)\right]E\left[W(t)\right]=E\left[e(t)\right] \tag{3.39}$$

Therefore, the expected value of the error signal should also be equal to zero which implies that Equation 3.37 reduces to the following:

$$E[e(t)X(t)] = -(m_e m_X + m) \tag{3.40}$$

Substituting Equation 3.38 into Equation 3.40 results in the following relation:

$$E[XRi_{mech} - XX^T q] = -(m_e m_X + m) \tag{3.41}$$

If the instantaneous mechanical response correlation with the reference signals is small, as in the case of large excitation bandwidth (see Figure 3.13), the expected value will be negligible. Because of the definition of R, Equation 3.41 can be rewritten as follows:

$$q = R^{-1}(m_e m_X + m) \tag{3.42}$$

Given the misadjustments in the weights, the excess mean squared error (MSE) can be calculated as well.

$$\begin{aligned} \|e(t)\|^2 &= E[e(t)e(t)] = E[q^T XX^T q] = E\left[(m_e m_X + m)^T R^{-T} R R^{-1}(m_e m_X + m)\right] \\ &= (m_e m_X + m)^T R^{-T}(m_e m_X + m) \end{aligned} \tag{3.43}$$

In Equation 3.43, it can be easily seen that the excess MSE is inversely related to the input correlation matrix. This implies that higher input powers, which increase the norm of R will reduce the excess MSE. Therefore, the circuit should be operated with as high an input power as possible without saturating the components to reduce the detrimental effects of DC offset error.

This analysis also stresses the importance of eliminating as many sources of DC offset as possible, which includes the null adjust on the LMS integrators. According to

Equation 3.42 it should be possible to eliminate all DC offset error using the LMS integrators' null adjust, but the complications involved in identifying the appropriate values of m to accomplish such a task is beyond the scope of this work. The author refers readers to the reference by Tzeng (1990) which demonstrates an adaptive technique for offset cancellation in a switched capacitor adaptive analog filter using an additional set of tap weights.

4. Experimental Setup and Results

4.1 Test Beam and Circuit Hardware Configuration

The apparatus used for the experiments was intentionally simple for ease of modeling and simplification of test procedure. The experimental smart structure was a 6061-T6 aluminum beam (17" x 1" x 0.062"), freely hanging with two PZT wafers bonded opposite each other, connected in series and poled 180 degrees out of phase to impose a local bending moment on the structure when actuated. The wafers were located at approximately one-quarter the length of the beam so that the first five modes (all below 800 Hz) could be observed. The first mode did not have an extremely strong amplitude response at this location and was nearly unobservable.

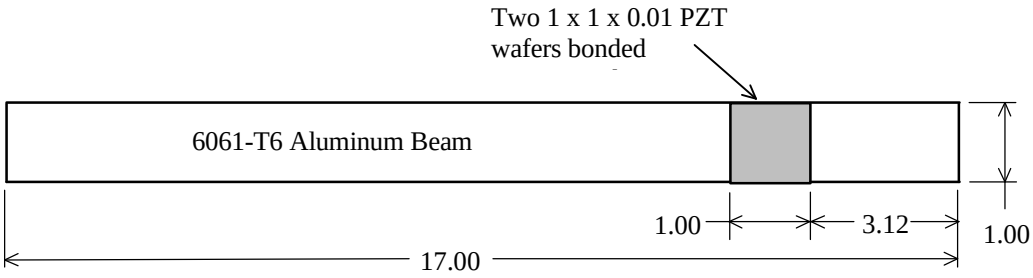

Figure 4.1 - Dimensions of test beam

The single-weight Sensoriactuator circuit shown in Figure 3.5 was breadboarded as was the two-weight adaptive circuit shown in Figure 3.12. Using these configurations,

the merits of the two-weight analog adaptive Sensoriactuator could be demonstrated by direct comparison.

4.2 Experimental Approach

A metric for comparison of the performance of the two different circuit configurations had to be established. Using the simple geometry of the free-free beam, it was possible to experimentally measure a nearly collocated response using one PZT as an actuator and the other PZT as a sensor. Since the two wafers were bonded directly opposite each other, and because the beam could be treated as an Euler-Bernoulli beam, meaning through-thickness stress is negligible compared to bending, the strain experienced by each PZT would be approximately equal and opposite that of the other. The overall actuation authority was reduced by using only one PZT, but this did not prove to be a problem for measuring the frequency response. Because of differences in the transfer functions due to the inconsistent piezoelectric capacitances of the two arrangements, the scaling of the measured FRF for the sensor/actuator arrangement did not coincide with that of the Sensoriactuator. Therefore, it merely serves as an estimate of the nature of a collocated response expected from the Sensoriactuator, not the exact magnitude. In order to compare sensor/actuator and Sensoriactuator FRFs, the sensor/actuator magnitude was scaled to match the gain calculated by the model.

Once a metric for comparison was established, several tests were run to demonstrate the following aspects of the circuit performance:

- adaptation to changing plant parameters

- effects of input signal power on adaptation
- effects of DC offsets on convergence

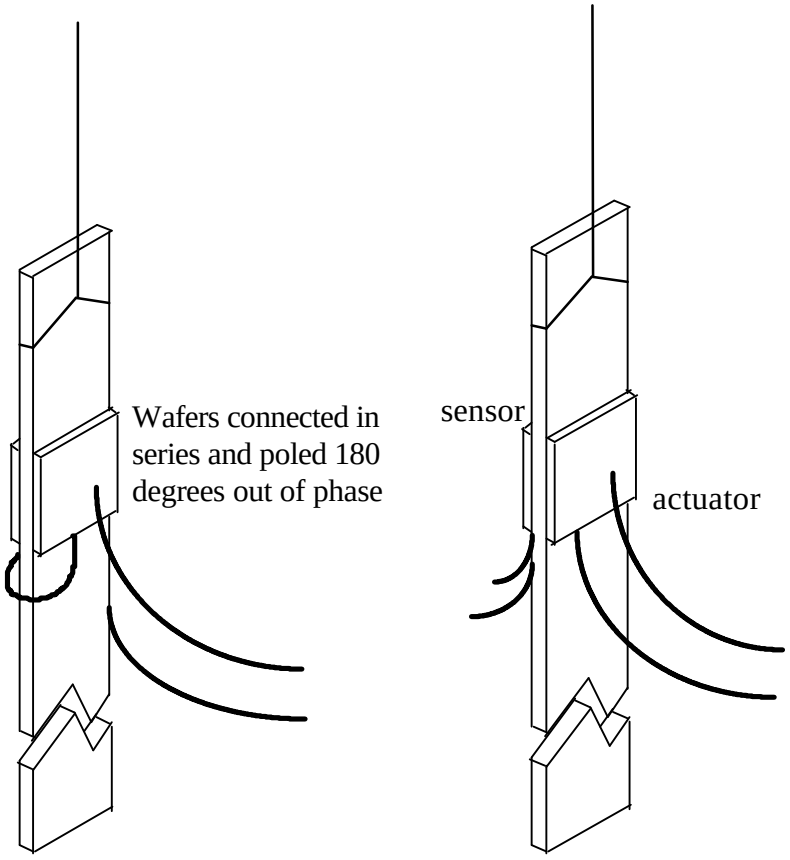

Figure 4.2 - Configurations for collocated and nearly collocated response measurements

4.3 Testing Procedures

The basic premise behind designing an adaptive corner frequency of the two-weight high-pass filter was that the capacitance of the PZT wafers can be expected to drift as a function of applied voltage and environmental conditions. The result is a change in

the corner frequency (i.e. the first-order dynamics) of the feedthrough electrical part of the piezoelectric response. If the adaptive filter could track this drift, then phase matching between the two branches of the circuit would not require special tuning, as with previous methods, but would be tuned adaptively.

Two tests were performed to demonstrate the flexibility and advantages in using the two-weight circuit. The first of these involved changing the piezoelectric capacitance by heating it with a hot air gun. Since piezoelectric capacitance is known to change as a function of temperature, this test represented a likely plant variation. Hot air was blown over the PZT wafers at a distance of approximately one inch for about 15 seconds. This heating caused a noticeable change in capacitance and the adaptive weights were recorded during the transient. FRFs are provided for the system before and after the heating for comparison of the circuits. Similarly, a second test was designed to show the adaptability to plant variations by abruptly shorting out one of the PZT's (see Figure 4.2) thereby causing a step change in capacitance. Again, the adaptive weights were recorded during the transient and FRF measurements taken both before and after the transient for comparison.

A second set of tests was designed to demonstrate the effects of input signal power on the adaptation. As described in Chapter 3, theory predicts that the DC offset error would be reduced by increasing the norm of the input correlation matrix. The adaptive weights were recorded using a variety of input signal strengths, and observed to change as a result. In these experiments, the weights strayed from the optimal values as input voltage was lowered, implying that the input voltage should be raised to reduce DC

offset error. However, if the input signal strength is too high, saturation occurs in the circuit components, causing a drop in coherence, and therefore filter convergence, due to the nonlinear response. Thus, the input magnitude should be made as high as possible without saturating any of the op-amps in the circuit.

Finally, the two adaptive circuits were tested with a DC offset added to the output (or error signal) to experimentally demonstrate the effects of offset error. The result of all these tests is shown in the following section.

4.4 Presentation of Results

In order to illustrate the signal-to-noise ratio between the feedthrough and mechanical response terms of the piezoelectric response, Figure 4.4 shows both the compensated and uncompensated Sensoriactuator response plots on similar axes in the time domain. FRFs of the same data are shown in Figure 4.5. The uncompensated response is dominated by the feedthrough electrical dynamics. The modal resonances of the beam are barely detectable in these predominantly first-order curves, corresponding to the magnitude and phase responses. The Sensoriactuator response curves appear along with the uncompensated response, some 20-25 dB below in magnitude. The Sensoriactuator phase plot contains only the structural phase response as well. This plot makes it easy to see the signal-to-noise ratio that has been elaborated on and obviates the sensitivity of this compensation scheme to relative phase matching errors in the reference leg of the compensator. If the relative phase between the electrical part of the piezoelectric output and the adaptive high-pass filter are not 180^{o} apart, then the

mechanical response will be difficult to resolve due to the high signal-to-noise ratio between the mechanical and electrical feedthrough responses.

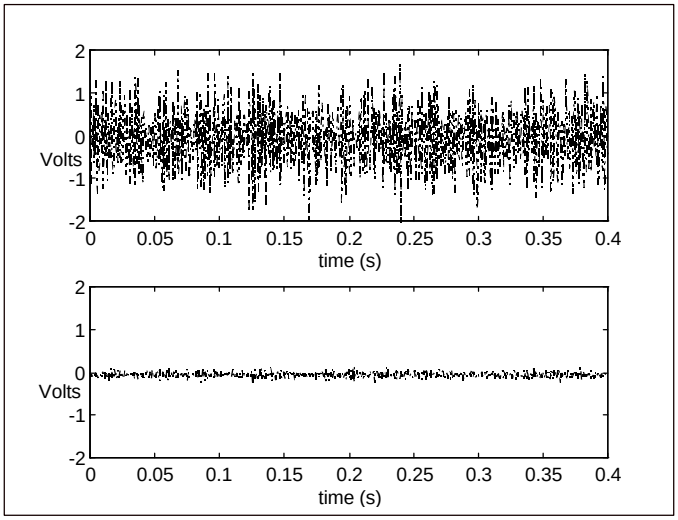

Figure 4.4 - Uncompensated and Sensoriactuator time responses

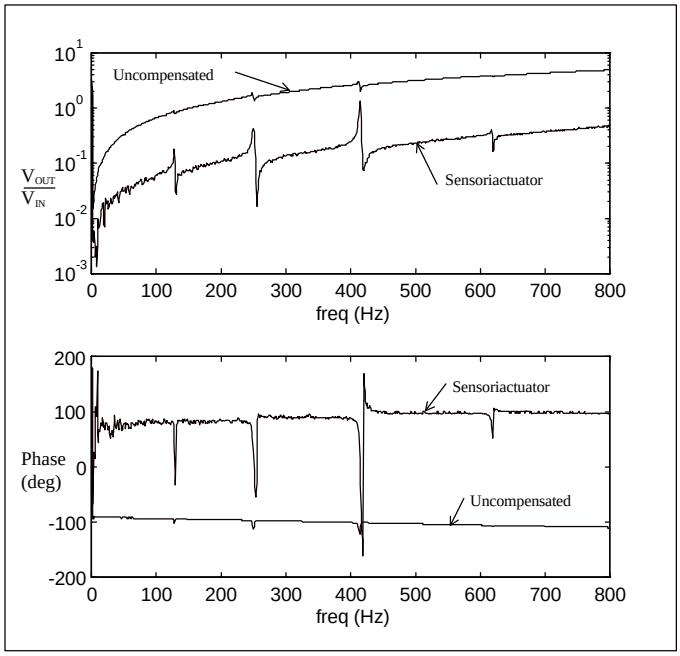

Figure 4.5 - Uncompensated and Sensoriactuator frequency responses

4.4.1 Performance Compared to Model and Sensor/Actuator Response

To establish a frequency domain metric of performance for the adaptive Sensoriactuator, a system model was created with a Rayleigh-Ritz formulation using the first fourteen free-free mode shapes of the unloaded beam. This numerical model follows the technique described by Hagood (1990) for modeling piezoelectric adaptive structures, and features a state space development which accounts for the distributed strain modal contribution of each PZT in the structure based on its geometrical location. The state space model was implemented in Matlab in an m-file called beam.m which appears in the Appendix. The experimental results of the single-weight and two-weight adaptive circuits are compared to the model in Figure 4.6 below. These figures show that both the adaptive configurations agree well with the model and sensor/actuator responses in both magnitude and phase.

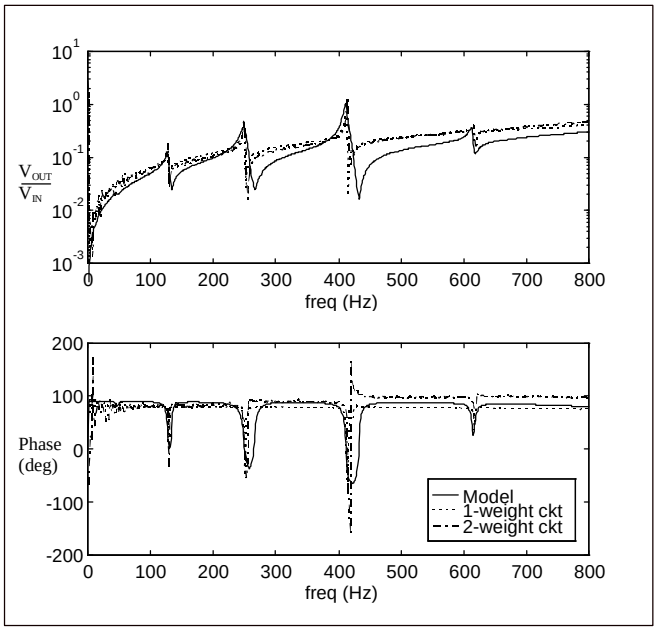

Figure 4.6 - FRFs of theoretical and experimental Sensoriactuator responses

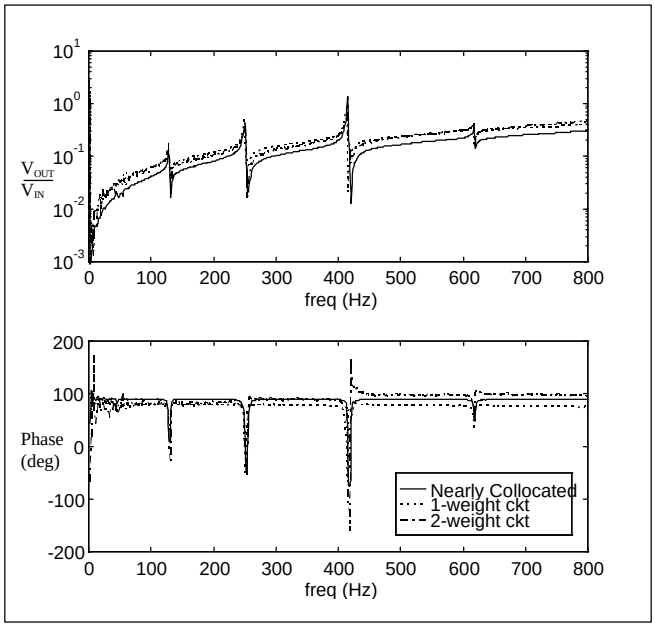

Figure 4.7 - FRFs of Sensoriactuator responses and scaled sensor/actuator response

4.4.2 Adaptation to Piezoelectric Plant Variations

The single-weight adaptive circuit was unable to successfully track the artificial plant variations imposed. In fact, the case of shorting one PZT was such a drastic change, that the adaptive weight immediately saturated. However, even the relatively mild change in C_P due to heating proved too much for the single-weight filter to accommodate. This is because changes in the piezoelectric capacitance change the corner frequency of the piezoelectric high-pass filter. Recalling that the corner frequency of the reference leg is not adaptable, the single-weight compensator is unable to accommodate even the slightest change in C_P. This result has implications for the previously implemented hybrid compensator as well. The change in C_P would alter the gain crossover frequency, thereby affecting the relative phase in the low frequency band, which would degrade its effectiveness.

The two-weight compensator, however, was able to track changes in C_P and re-adapt its corner frequency to compensate the new first-order dynamics of the feedthrough electrical term. Even the abrupt change in C_P brought on by shorting one PZT was successfully compensated as can be seen in the figures that follow. The adaptive weights converged within one second of the step change in C_P. Clearly, the capability of the two-weight compensator to change the corner frequency of its high-pass filter is an advantage for effective Sensoriactuator performance.

Table 1 shows the expected and observed gains of the actual VCAs in the adaptive circuit, G_A and G_B, before and after the abrupt change in C_P. The expected values were

calculated by matching the gains $A=15*G_A$ and $B=2595*G_B$ of the adaptive filter to the nominal gains R_1/R_{C1} and $1/(R_1C_P)$ of the piezoelectric circuit as in Eqs. 3.12 and 3.13. The numbers multiplying G_A and G_B are due to the amplification of the final summing amplifier and the nominal gain of the integrator in the adaptive filter as discussed in Section 3.4. Knowing that the sensitivity of each VCA was -33mV/dB, and that a zero control voltage corresponds to a nominal gain of 20dB for the arrangement shown in Figure 3.7, it was possible to calculate the values shown below based on the nominal resistance values in Figure 3.12 and by knowing that C_P went from 31.4 nF to 56.6 nF when one wafer was shorted.

Table 4.1. Expected and Observed Adaptive Filter Gains for a Shorted Piezoelectric Wafer.

	Before Short		After Short	
	Expected	Observed	Expected	Observed
G_A	0dB	0.21dB	0dB	1.27dB
G_B	14.85dB	15.45dB	9.70dB	11.45dB

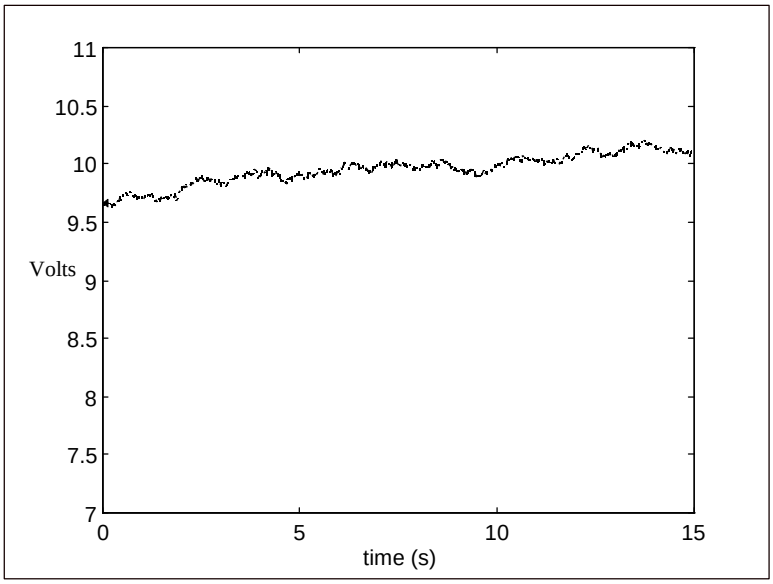

Figure 4.8 - Adaptive weight of single-weight adaptive filter during heating

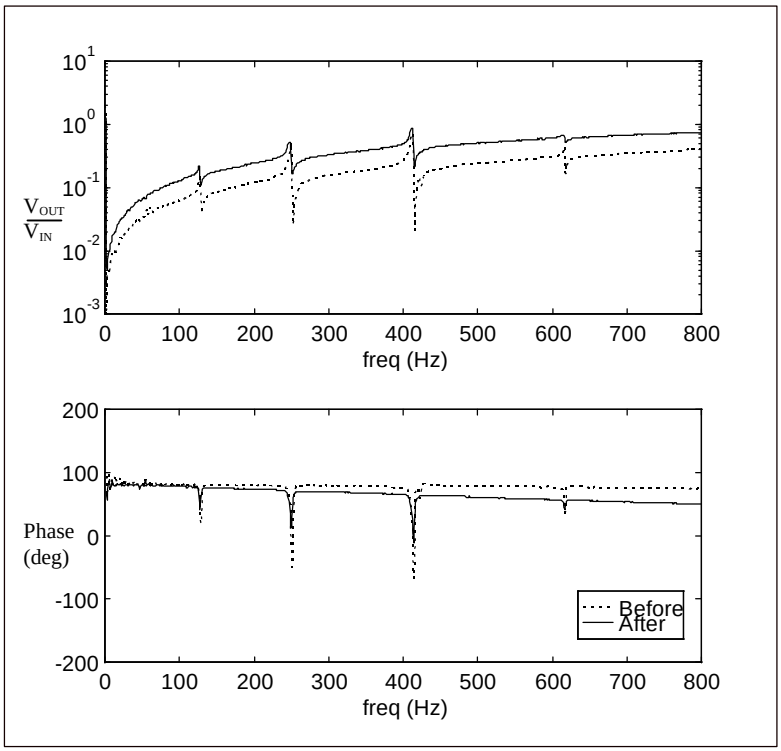

Figure 4.9 - FRF of single-weight circuit before and after gradual capacitance change

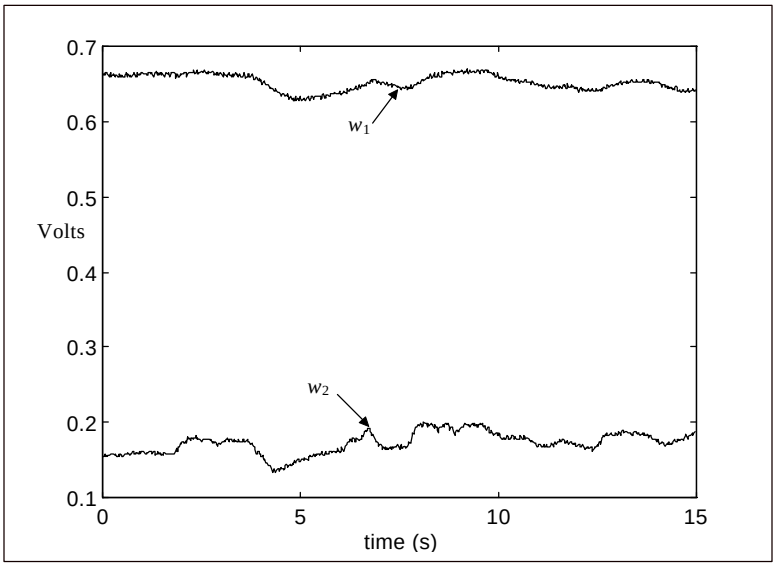

Figure 4.10 - Adaptive weights of two-weight adaptive filter during heating

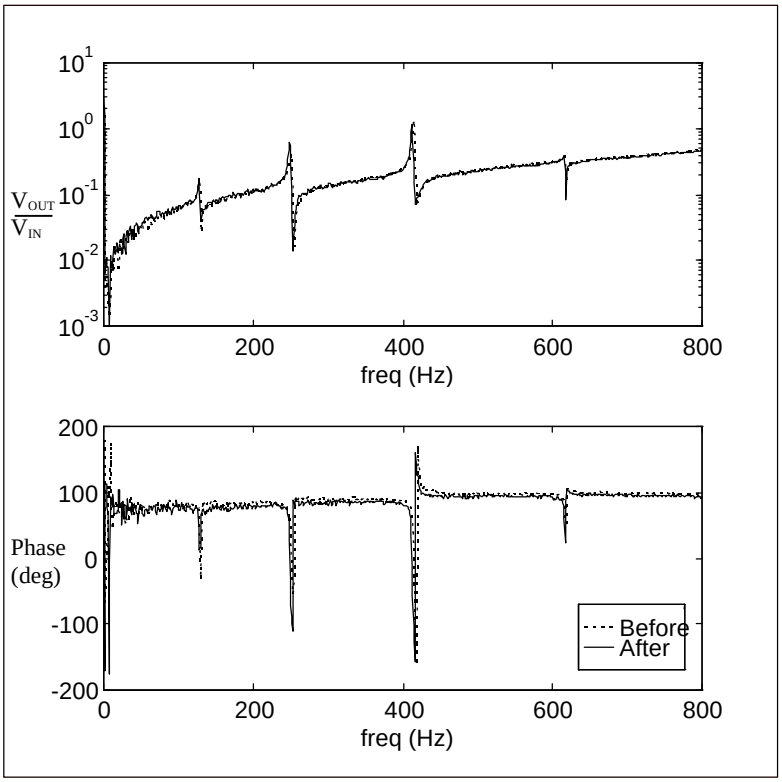

Figure 4.11 - FRF of two-weight circuit before and after gradual capacitance change

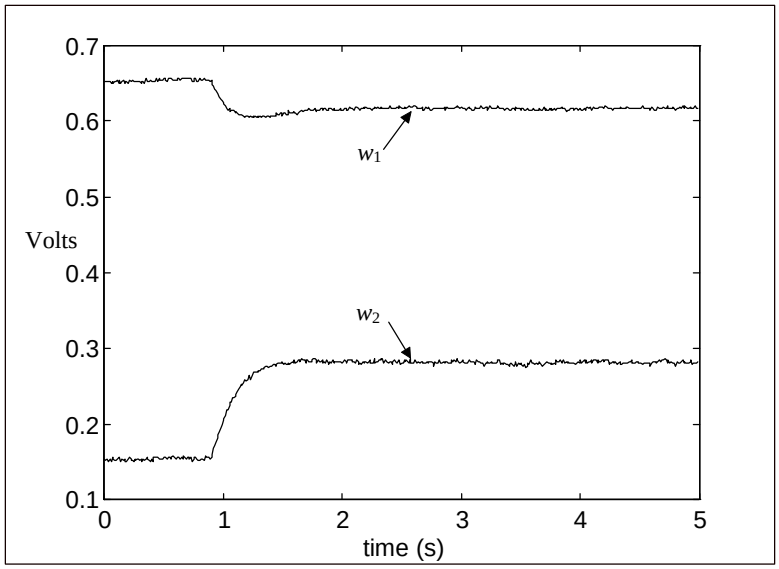

Figure 4.12 - Adaptive weights of two-weight filter for abrupt capacitance change

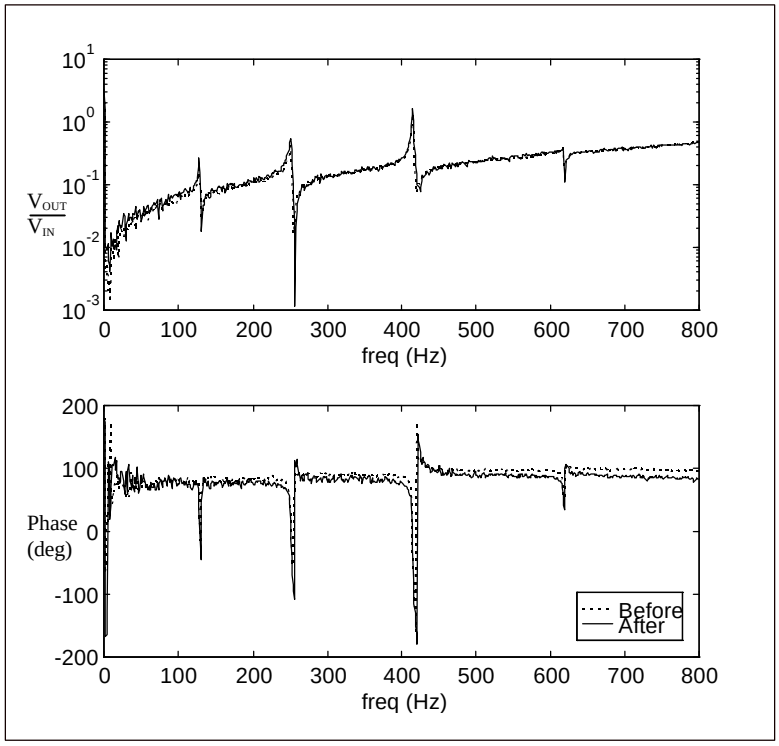

Figure 4.13 - FRF of two-weight circuit before and after abrupt capacitance change

According to the values shown in Table 4.1, the adaptive circuit behaved as expected. However, there were small discrepancies between expected and observed results that deserve some explanation. A portion of this variation may be due to DC offsets present in the system or to the small amount of bias in the optimal weights. As mentioned previously, the analog adaptive configuration is susceptible to DC offset errors. Recognizing this, experiments were performed to demonstrate how DC offsets can degrade adaptive system performance.

4.4.3 Effects of DC Offsets on Adaptation

In order to show how DC offsets can cause the system to adapt improperly, the following experiments were performed with the two adaptive compensators. First, artificial DC offsets were introduced at the error signal and the resulting adaptation measured. Referring to Equation 3.41, it is easy to see that DC offset on the error signal will cause the weights to become misadjusted. Similarly, misadjustment in the weights will increase as the inverse of the input correlation matrix, R. Since input signal power affects the adaptation as well, a second series of experiments was performed to demonstrate the effects of input signal strength on adaptation. The results of these two tests are presented in the plots and FRFs below.

Figures 4.14 and 4.15 show the effects of adding a DC offset directly to the error signal of the adaptive filter. The weights misadjust and the phase response of the Sensoriactuator is degraded as DC offset increases. Similarly, when the input correlation

matrix norm is reduced (i.e. as the voltage level of the excitation is reduced), the Sensoriactuator performance degrades as shown in Figures 4.16 and 4.17. Figure 4.18 and 4.19 show how the single-weight adaptive filter performed with decreasing input voltage. Both adaptive circuit configurations' magnitude response suffered when the input level was decreased.

It is easy to see that the adaptation of the two-weight circuit is sensitive to DC offset error, and therefore precautions should be taken to reduce them. The first and easiest thing to do is to raise the input power to the maximum level allowable without saturating the circuit components. Second, DC offsets can be reduced by null adjusting the LMS integrators. These steps have been mentioned previously, but they bear repetition as they are very important for optimal Sensoriactuator performance. In addition, the null offset of the adaptive filter integrator should probably be adjusted as not to add DC offsets to $X_2(t)$, though for these experiments, it was not, and remains as a potential contributor to errors in the converged weight values.

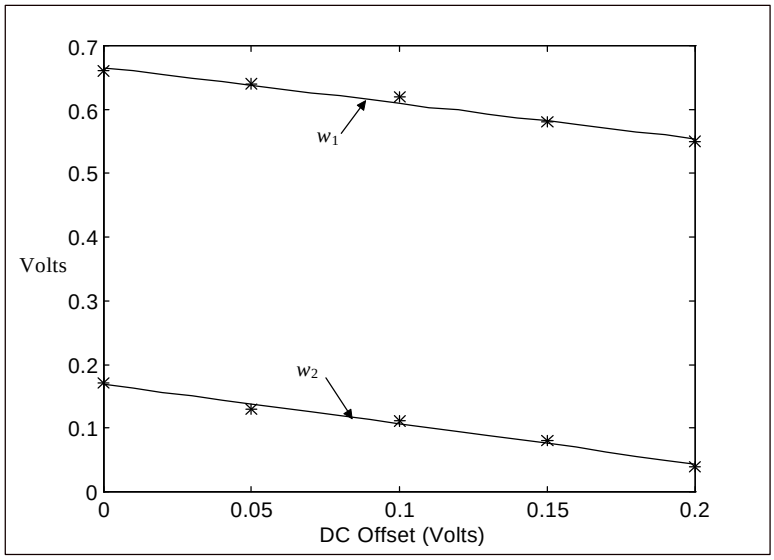

Figure 4.14 - Variation in adaptive weights for two-weight compensator as a function of DC offset added to the error signal

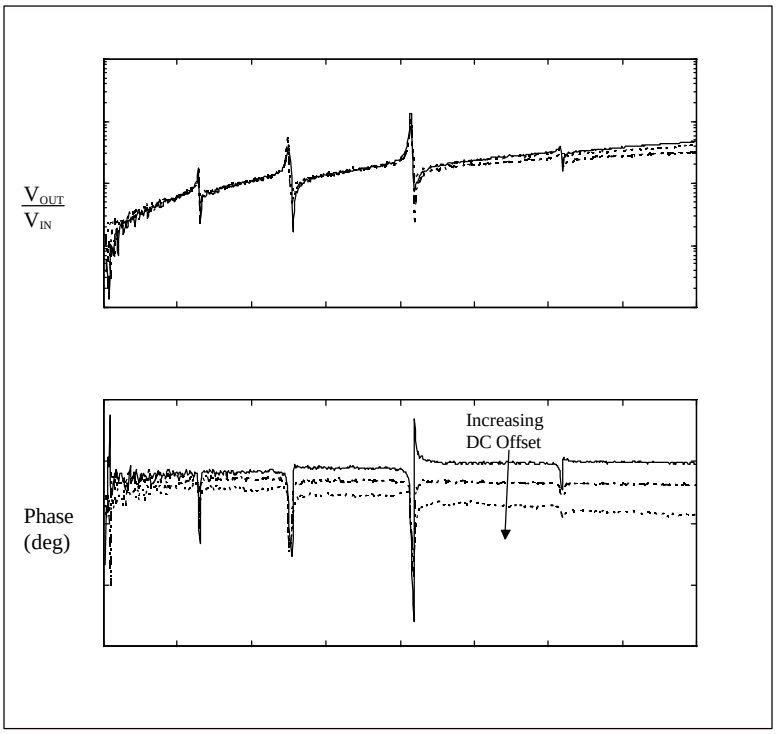

Figure 4.15 - FRFs of Sensoriactuator with DC offset on the error signal

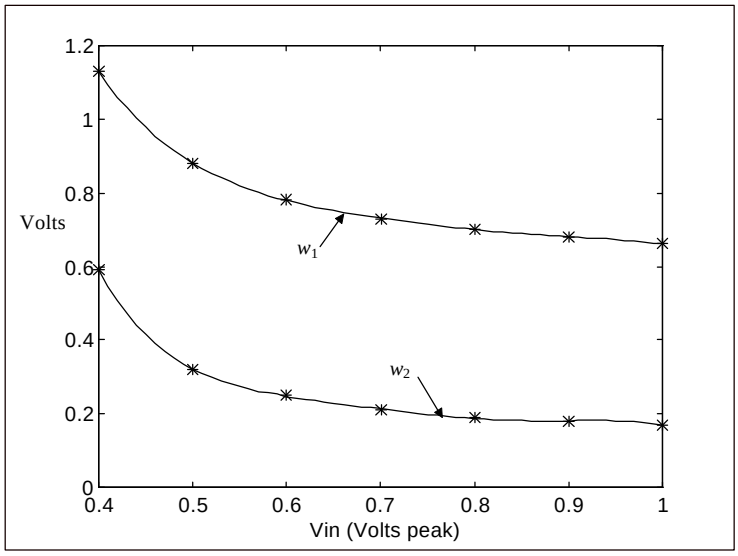

Figure 4.16 - Variation in adaptive weights for two-weight compensator as a function of white noise input voltage peak value

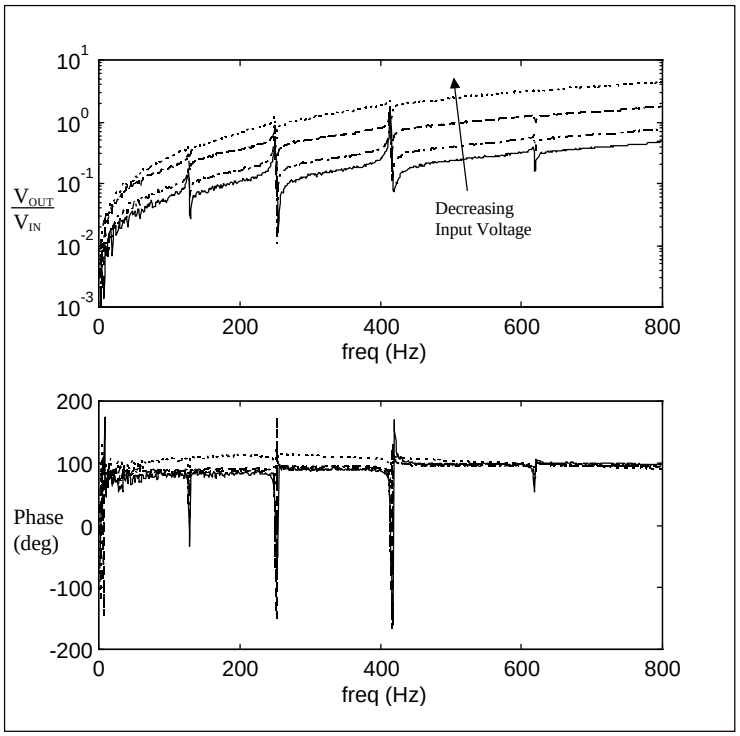

Figure 4.17 - FRFs of Sensoriactuator with varying input voltages

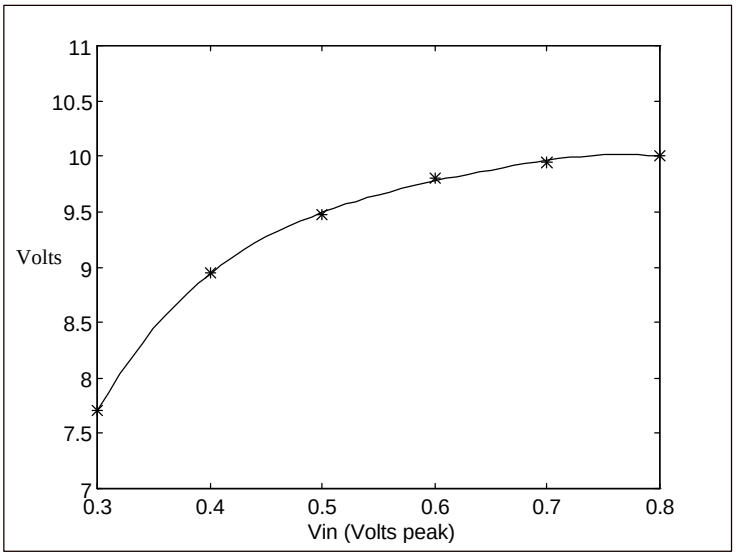

Figure 4.18 - Variation in adaptive weights for one-weight compensator as a function of white noise input voltage peak value

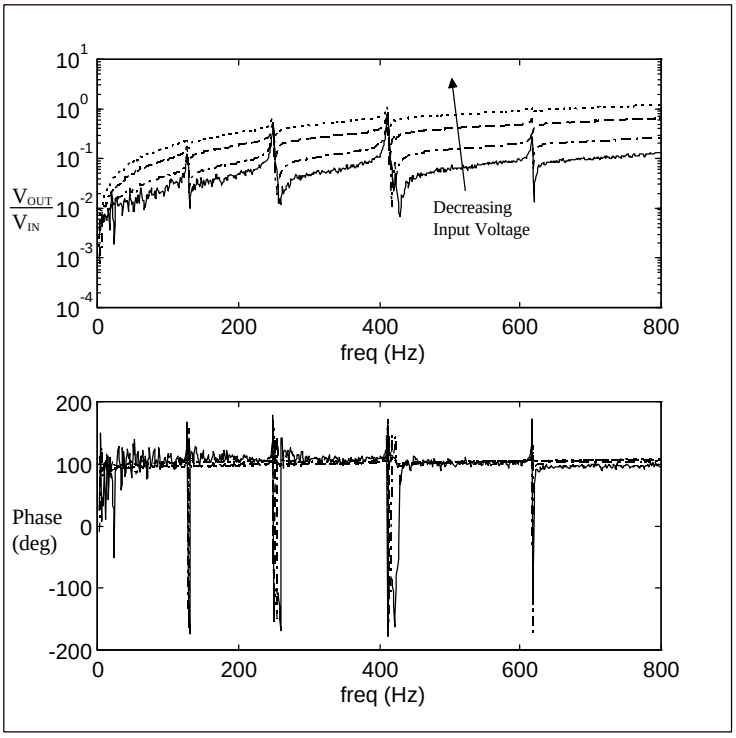

Figure 4.19 - FRFs of Sensoriactor with varying input voltages

5. Conclusions and Future Work

5.1 Final Summary

A circuit has been proposed which adaptively compensates the first-order feedthrough dynamics of a piezoelectric Sensoriactuator by matching the first-order properties with an adaptive high-pass filter. The adaptive compensation scheme was shown to adequately compensate the feedthrough current for strain rate measurements and moves away from previous implementations based on differentiation. The adaptive compensator was shown theoretically and experimentally to converge to the desired result of matching the corner frequency and gain of the high-pass feedthrough dynamics with an adaptive filter provided the input excitation bandwidth sufficiently minimized mechanical correlation bias on the adaptive filter weights.

Additionally, the two-weight circuit demonstrated a capability to track variations in the piezoelectric capacitance, re-adapting despite drastic plant variations. Its sensitivity to DC offset error was theoretically derived and demonstrated with qualitative comparisons of FRFs of the circuit being subjected to artificially imposed offsets. These results stress the importance of minimizing DC offsets during implementation. The two-weight adaptive circuit design proved more flexible, simpler to build, and the analog LMS

was less costly than previous adaptive implementations which required DSP hardware to run the adaptive algorithm. However, during the course of this research, several aspects of the design showed to be less than optimal, and deserve further attention.

5.2 Future Work

As mentioned previously, the circuit designed and implemented for this research was expressly for the purpose of experimental system identification. However, collocated strain rate response is ideal for closed loop control applications, especially for flexural vibration control in adaptive structures. The problem with using this circuit for such an application is that the piezoelectric wafer is used as a capacitive circuit element and the voltages applied to it will be applied also to a breadboard full of solid state electronic components which are unable to handle the high voltages (100+ Volts) required for structural control. A technique must be developed where the piezoelectric element is isolated from the electronics, but its dynamics are kept accessible to the adaptive circuitry. Preliminary studies have been conducted with this type of application with promising results.

5.2.1 High Voltage Sensoriactuator

Fortunately, a piezoelectric wafer, forced by an excitation voltage acts like a high-pass filter when the output is measured across a resistor, as the circuit diagram below indicates. Thus, we don't need to include the PZT in an active op-amp filter to observe first-order dynamics. This is a great advantage for the high voltage application since we

can observe the dynamics by using a simple voltage divider to monitor a small fraction of the total output voltage for the adaptive circuitry.

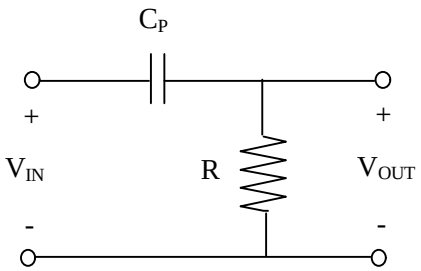

$$\frac{V_{OUT}(s)}{V_{IN}(s)} = \frac{RC_P s}{1 + RC_P s}$$

Figure 5.1 - Passive piezoelectric high-pass filter

Through judicious choice of R, the piezoelectric high-pass filter can act like a differentiator in the low frequency band, and the signal across the resistor can be attenuated enough to be fed into an isolation amplifier. The excitation voltage, V_{IN}, can be divided using a potentiometer and sent into an isolation amplifier to generate the input voltage for the adaptive circuitry. A schematic of such a system is shown in Figure 5.1. Since the voltage drop across R should be small compared to V_{IN}, the piezoelectric wafer sees a comparatively large voltage, which is desired for structural control authority.

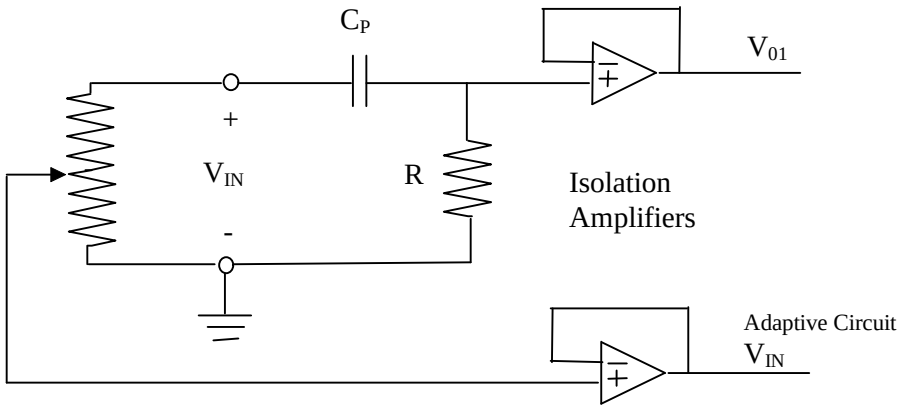

Figure 5.2 - Isolation scheme for high voltage Sensoriactuator

This configuration has been tested briefly, but without serious consideration of the circuit design and dynamics. In order for this implementation to work well, the adaptive circuit should be designed to operate nominally around the dynamics of this particular piezoelectric high-pass filter gain set, just as the previous circuit was designed. Recall that the adaptive circuit was designed so that the VCAs operated nominally near unity gain, and that this was accomplished through judicious choices of resistors and capacitors in the op-amps of the adaptive high-pass filter. The same procedure would have to be followed for this circuit in order to prevent operation near the extreme limits for the VCAs where their performance would degrade.

5.2.2 Adaptive Sensoriactuator for Collocated Rate Feedback Control

Structural vibration control using collocated rate feedback would be feasible with the development of a high voltage Sensoriactuator. However, the adaptive circuitry requires white noise excitation, for proper adaptation. Therefore, the design issue for

application to feedback control is the adaptation of the weights. When the control signal is input to the piezoelectric wafer, the circuit is no longer being excited by white noise, and the weights will misadjust, causing the output response to contain other than mechanical strain rate information. From a control design perspective, the robustness of this control scheme would be very poor, since the feedback signal would be very noisy.

In order to alleviate the problem, the adaptive weights could be periodically trained with a low level white noise source, with feedback control momentarily disengaged, then have the weights held constant while using the control. One method could be to short the inputs of the LMS integrators to ground, thereby freezing their outputs on the correct adaptive weight values while control is active. This arrangement would require switching circuitry which could be automated with a micro-controller circuit, or simple clock timing. A white noise source would also be required. The method would depend on precise null adjustment of the LMS integrators, so that the frozen weights wouldn't change when the integrator inputs are grounded. Integrator null adjustment would then serve the dual purposes of minimization of offset error during adaptation and holding weight values constant during application of control.

5.2.3 Redesign of Adaptive Filter Using Analog Multipliers

Another issue for future work is the design of the adaptive filter electronic components. Originally, VCAs were used because of their large dynamic range which would accommodate the large adaptation gains in the high-pass filter. However, after practical experience with the VCA-based circuitry, it was found that the VCAs should

ideally be operated near unity gain. Therefore, the adaptive high-pass filter was designed to accommodate that requirement.

In retrospect, the circuit could have been designed the same way using analog multipliers in place of the VCA gain blocks, where the adaptive weights would then be the gains and the whole circuit would require less components and would operate without the added dynamics of the VCA chips and supporting op-amps. During the course of designing and testing this circuit, many VCA chips were destroyed by an LMS integrator saturating the command voltage and demanding far more gain than the VCA was designed to provide. The adaptation gains easily strayed out of the linear range of operation during startup and at times during operation, resulting in a command voltage saturation, which was disastrous for the VCAs.

It is anticipated that clever design with analog multipliers and accompanying adaptive high-pass filter components will result in a circuit that operates in a linear range more of the time, thereby making the system more robust. It would be ideal if even a saturated LMS weight (+/- ~15 Volts) kept the circuit in the linear range of operation, thus making nonlinear operation of the adaptive filter (i.e. saturation) impossible. Because of the large dynamic range of the VCAs for a small range of command voltages, the overall linear range of operation for the adaptive circuit was relatively narrow with respect to the possible LMS integrator voltage outputs. Anything beyond about ±2 volts was too large for the VCAs.

A possible tradeoff with using analog multipliers could be the significant reduction of dynamic range per volt of adaptive weight. The circuit design will have to operate

nominally at the correct solution with allowable ranges extending several dB above and below that value. What voltage value for the adaptive weights should be chosen as the nominal value? Will too low an amplification voltage cause problems with noise? These are considerations that must be made in using such a design. It is the opinion of the author, however, that a design which makes use of analog multipliers in place of the VCAs will be more robust and simpler to use.

References

Anderson, E. H., N. W. Hagood and J. M. Goodliffe. 1992. "Self-Sensing Piezoelectric Actuation: Analysis and Application to Controlled Structures," AIAA-92-2465-CP.

Cole, D. G. and R. L. Clark. 1994. "Adaptive Compensation of Piezoelectric Sensoriactuators," *J. of Intell. Mater. Syst. and Struct*, Vol. 5, Sept., pp. 665-672.

Cole, D. G., W. R. Saunders, and H. H. Robertshaw. 1995. "Modal Parameter Estimation for Piezostructures," *Journal of Vibration and Acoustics - Transactions of the ASME*, Vol. 117, No. 4, Oct., pp. 431-438.

Crawley, E. F., deLuis, J. 1987. "Use of Piezoelectric Actuators as Elements of Intelligent Structures," *AIAA Journal*, Vol. 25, No. 10, Oct., pp. 1373-1385.

Dosch, J. J., D. J. Inman and E. Garcia. 1992. "A Self-Sensing Piezoelectric Actuator for Collocated Control," *J. of Intell. Mater. Syst. and Struct*, Vol. 3, January, pp. 166-185.

Franco, S. 1988. *Design with Operational Amplifiers and Analog Integrated Circuits*, New York: McGraw-Hill, Inc.

Hagood, N. W., W. H. Chung and A. von Flotow. 1990. "Modeling of Piezoelectric Actuator Dynamics for Active Structural Control," AIAA-90-1087-CP.

Johns, D. A., W. M. Snelgrove, and A. S. Sedra. 1991. "Continous-Time LMS Adaptive Recursive Filters," *IEEE Transactions on Circuits and Systems*, Vol. 38, No. 7, July, pp. 769-777.

Johns, D.A., W.M. Snelgrove, and A.S. Sedra. 1989. "DC Offsets in Analogue Adaptive IIR Filters," IEE Conference Publication No. 308, *European Conference on Circuit Theory and Design*, pp. 137-141

Karni, S. and G. Zeng. 1989. "The Analysis of the Continuous-Time LMS Algorithm," *IEEE Transactions on Acoustics, Speech, and Signal Processing*, Vol.37, No.4, pp. 595-597.

Meirovitch, L. 1986. *Elements of Vibration Analysis*, Second Edition. New York: McGraw-Hill, Inc.

Newland, D. E. 1993. *An Introduction to Random Vibrations, Spectral & Wavelet Analysis*, Third Edition. Essex: Lomgman Scientfic & Technical.

Piezo Systems Product Catalog, Piezo Systems, Inc., Cambridge, MA. 1994

Saunders, W. R., D. G. Cole, and H. H. Robertshaw. 1994. "Experiments in Piezostructure Modal Analysis for MIMO Feedback Control," *J. Smart Mater. Struct*, Vol. 3, pp. 210-218.

Saunders, W. R., D. G. Cole, and C. A. Fannin. 1996. "Similitude Analyses for Piezostructures," *J. of Intell. Mater. Syst. and Struct*, Vol. 7, March, pp. 162-167.

Shoval, A., D. A. Johns, and W. M. Snelgrove. 1995. "Comparison of DC Offset Effects in Four LMS Adaptive Algorithms," *IEEE Transactions on Circuits and Systems*, Vol. 42, No. 3, pp. 176-185.

Vipperman, J. S. and R. L. Clark. 1995. "Hybrid Analog and Digital Adaptive Compensation of Piezoelectric Sensoriactuators," AIAA-95-1098-CP.

Widrow, B., P. E. Mantey, L. J. Griffiths, and B. B. Goode. 1967. "Adaptive Antenna Systems," *Proceedings of the IEEE*, Vol. 55, No. 12, December, pp. 2143-2159.

Widrow, B. and S. D. Stearns. 1985. *Adaptive Signal Processing*, Englewood Cliffs: Prentice-Hall, Inc.

Appendix

This appendix contains all the Matlab m-files that were used for modeling the beam dynamics along with the m-file that generated Figure 3.13 showing the effect of mechanical response correlation on the bias in the adaptive weights.

The first file is called beam.m and must be accompanied by testbeam.m and the functions shape.m and strain.m which follow. This is the file which contains the Rayleigh-Ritz beam dynamic model. The m-file was originally written by Dan Cole, but has been significantly modified from its original form for use in this research. Among other things, the mode shape integration scheme changed, significantly reducing run time.

BEAM.M

```
%   This m-file sets up the mass, stiffness etc. matrices
%   to be used in the state space model for a free-free beam.

%   The beam is modeled using Bernoulli-Euler beam mode shapes.
%   Six mode shapes are used in this model.


% example variables ====================================================
m      = 21;                        % number of modes
n      = 1;                         % number of PE
z      = [0.05 0.02 0.02 0.008 0.005 0.1*ones(1,m-5)];  % damping coefficient vector
cs     = 69e9;                      % structure stiffness (Pa)
rhos   = 2710;                      % density of Al (kg/m3)
rhop   = 7750*ones(1,n);    % density of PE (kg/m3)
cp     = 6.2e10*ones(1,n);        % stiffness of PE (Pa)
d31    = 170e-12*ones(1,n);       % electro-mechanical coupling coefficient
ep     = cp.*d31;           % piezo material const. relates volts-3dir to sigma-1dir
eep    = 1700*8.85e-12*ones(1,n); % emissivity of PE
testbeam;

% ======================================================================

voltage = [.5]';             % input patch voltage
global wl nmc
kl = [4.7300407 7.8532046 10.9956078 14.1371655 17.2787597 20.4203522 23.561945 ...
```

```
    26.7035376 29.8451302 32.9867229 36.1283155 39.2699082 42.4115008 45.5530934 ...
    48.6946861 51.8362788 54.9778714 58.1194641 61.2610567 64.4026494 67.5442421];
%    70.6858347 73.8274274 76.9690200 80.1106127 83.2522053 86.3937980 89.5353906 ...
%    92.6769833 95.8185759 98.9601686 102.101761 105.243354 108.384947 111.526539 ...
%    114.668132 117.809725 120.951317 124.092910 127.234502 130.376095 133.517688];

wl   = kl/length; % "wave numbers"
nmc = -(cosh(kl)-cos(kl))./(sinh(kl)-sin(kl)); % "normal mode coefficients"

disp('calculating O')


% the following routine calculates the integral
% of the mode shape using a closed form.
O = zeros(m,n);
for i = 1:n
  for j = 1:m
     I =     sinh(wl(j)*ap(i,2))-sinh(wl(j)*ap(i,1));
     I = I -            (sin( wl(j)*ap(i,2))-sin( wl(j)*ap(i,1)));
     I = I +nmc(j)*( cosh(wl(j)*ap(i,2))-cosh(wl(j)*ap(i,1)) );
     I = I +nmc(j)*( cos(wl(j)*ap(i,2))-cos(wl(j)*ap(i,1)) );
    O(j,i) = (ep(i)*Sp(i)*wl(j)/tp(i))*I;
  end
end

Ms = rhos*As*length*eye(m,m);   % mass mx of the structure

disp('calculating Mp')

Mp = zeros(m,m);

for k = 1:n
 x=[ap(k,1):.0001:ap(k,2)]';
 sx=size(x);
 for i = 1:m
   for j = i:m
     y = shape(i,j,x,nmc,wl);
    I(i,j) = (x(sx(1))-x(1))/(sx(1)-1)*(sum(y)-y(1)/2-y(sx(1))/2);
   end
 end
 Mp=Mp+rhop(k)*Ap(k)*(I+I'-diag(diag(I),0));
end

Ks = cs*Is*length*diag(wl(1:m).^4,0);

disp('calculating Kp')

Kp = zeros(m,m);

for k = 1:n
 x=[ap(k,1):.0001:ap(k,2)]';
```

```
  sx=size(x);
  for i = 1:m
    for j = i:m
      y = strain(i,j,x,nmc,wl);
      I(i,j) = (x(sx(1))-x(1))/(sx(1)-1)*(sum(y)-y(1)/2-y(sx(1))/2);
    end
  end
  Kp=Kp+cp(k)*Ip(k)*(I+I'-diag(diag(I),0));
end

disp('here')
Cp = diag(eep.*Area./tp,0);

M = Ms+Mp;
K = Ks+Kp;
%K = Ks;                    % ignore stiffness from piezo
%M = Ms;

% add damping
A = [zeros(m,m),eye(m,m);-M\K,zeros(m,m)];
wn = sort(imag(eig(A)));
wn = wn(m+1:2*m);
A(m+1:2*m,m+1:2*m) = -2*diag(z,0).*diag(wn,0);

B = [zeros(m,1);M\(O*voltage)];
C = [O',zeros(n,m)];                    % outputs as charges (~ strain)
%C = [eye(m,m),zeros(n,m)];             % outputs are modal coordinates
D = zeros(n,1);
D2 = Cp*voltage;                        % feedthrough capacitance

%save mass14 M Ms Mp
%save stiff14 K Ks Kp
%save couple14 O
%save cpctnc14 Cp
%save pmodel A B C D
%clear
%load pmodel66

w = linspace(0,800*2*pi,800);
[magnitude,phase] = bode(A,B,C,D,1,w);
G1=magnitude.*(cos(phase*pi/180) + sin(phase*pi/180)*sqrt(-1));
[magnitude2,phase2]=bode(A,B,C,D2,1,w);
G2=magnitude2.*(cos(phase2*pi/180) + sin(phase2*pi/180)*sqrt(-1));
figure(2);clf;
semilogy(w/(2*pi),abs(G1(:,1)*sqrt(-1).*w')*32e3*1.5,'--',w/(2*pi),abs(G2(:,1)*sqrt(-1).*w')*32e3*1.5,'--
')
hold on;
%semilogy(freq,abs(dpfrf),'r');semilogy(freq,abs(uncomp),'g');
  % output as currents (~strain rate)
%semilogy(w,abs(G1(:,2)),w,abs(G2(:,2)),'--')
  % output as charge (~strain)
```

```
%title('FRF plots with unit input at patch 1')
```

TESTBEAM.M

```
tp     = 0.000254*ones(1,n);         % thickness of the PE (m)
Ap     = 12.903e-6*ones(1,n);        % cross sectional area of the PE (m2)
Sp     = 12.290e-9*ones(1,n);        % first area moment (m3)
Ip     = 11.776e-12*ones(1,n);       % area moment of interia of PE (m4)
length = 0.4318;                          % length of the beam (m)
As     = 41.935e-6;                   % cross sectional area of the beam (m2)
Is     = 9.526e-12;                   % area moment of inertia of the beam (m4)
xl     = length*[0.183]';         % one patch configuration
xr     = xl + .0254;
ap     = [xl' xr'];               % end points of the PE (m)
Area   = (0.0254)^2*ones(1,n);       % surface area of PE   m^2
```

SHAPE.M

```
function y = shape(i,j,x,nmc,wl)
y1=cosh(wl(i)*x)+cos(wl(i)*x)+nmc(i)*(sinh(wl(i)*x)+sin(wl(i)*x));
y2=cosh(wl(j)*x)+cos(wl(j)*x)+nmc(j)*(sinh(wl(j)*x)+sin(wl(j)*x));
y = y1.*y2;
```

STRAIN.M

```
function y = strain(i,j,x,nmc,wl)
y1=cosh(wl(i)*x)-cos(wl(i)*x)+nmc(i)*(sinh(wl(i)*x)-sin(wl(i)*x));
y2=cosh(wl(j)*x)-cos(wl(j)*x)+nmc(j)*(sinh(wl(j)*x)-sin(wl(j)*x));
y = wl(i)^2*wl(j)^2*y1.*y2;
```

CROSSCOR.M

```
% this m-file is used to calculate the cross-correlations
% of the desired to reference inputs for my Sensoriactuator
% using the analytical and numerically integrated results

clear;
R1=33e3;R2=2.2e3;Cp=31.4e-9;
A=R1/R2; B=inv(R2*Cp);var=1e-3;

O = [0.00105706867638
  0.00544924509642
  0.01249876612024
```

```
  0.01593291139507
  0.00768461612329
 -0.01498389239509
 -0.04401723685365
 -0.06193267163882
 -0.05097681394454
 -0.00553635100738
  0.06006202634483
  0.11474914846698
  0.12529596228608
  0.07542884569186
 -0.02138061932669
 -0.12413786059129
 -0.18248623269514
 -0.16247833163166
 -0.06628310076498
  0.06573724703253
  0.17317687435787];

wr =  1.0e+004 *  [0.02906347931534
  0.08042193103744
  0.15684016973914
  0.25865763944275
  0.38549276623340
  0.53780161922847
  0.71799686696517
  0.92469578986597
  1.15303815095995
  1.40524829885146
  1.68982366050926
  2.00538762529227
  2.34053185006245
  2.69138550969533
  3.07209532328000
  3.48985722260094
  3.93387569393556
  4.39488639264095
  4.87924152587050
  5.39441301274281
  5.93650763586081];

z     = [0.05 0.02 0.02 0.008 0.005 0.1*ones(1,16)]';

% theoretical
for n=1:5           % index for excitation frequency
  w1=2^n*200*pi;f(n)=w1/(2*pi);
 % calculate the input correlation matrix
  R = [var -A*var/(2*i*w1)*log((B+i*w1)/(B-i*w1));-A*var/(2*i*w1)*log((B+i*w1)/(B-i*w1))
A^2*var/(2*w1*B*i)*log((B+i*w1)/(B-i*w1))];
 % calculate the non-mechanical correlations of the P vector and calculate optimal Wiener weights
  P = [A*var+A*B*var*i/(2*w1)*log((B+i*w1)/(B-i*w1));0];
```

```
  W1(:,n) = inv(R)*P;
 % calculate the mechanical correlations for the P vector and add to P
  temp1=-R1*var*O.^2*i/(2*w1).*(i/2*log( (wr.^2-w1^2+2*w1*z.*wr*i)./(wr.^2-w1^2-2*w1*z.*wr*i) )
+ z./(2*sqrt(1-z.^2)).*log( (w1^2+wr.^2.*sqrt(1-z.^2)+z.^2.*wr.^2+2*w1*wr.*sqrt(1-
z.^2))./(w1^2+wr.^2.*sqrt(1-z.^2)+z.^2.*wr.^2-2*w1*wr.*sqrt(1-z.^2))));
  temp2=A*R1*O.^2*var/(2*w1).*( B./(B^2+2*B*z.*wr+wr.^2).*log((w1-B*i)/(-w1-B*i)) - (wr.*sqrt(1-
z.^2)-z.*wr*i)./(2*(i*wr.^2-z.^2.*wr.^2*i+wr.*sqrt(1-z.^2).*(wr.*z+B))).*log((w1-wr.*sqrt(1-
z.^2)+z.*wr*i)./(-w1-wr.*sqrt(1-z.^2)+z.*wr*i)) - (-wr.*sqrt(1-z.^2)-z.*wr*i)./(2*(i*wr.^2-z.^2.*wr.^2*i-
wr.*sqrt(1-z.^2).*(wr.*z+B))).*log((w1+wr.*sqrt(1-z.^2)+z.*wr*i)./(-w1+wr.*sqrt(1-z.^2)+z.*wr*i)) );
  P = P + [sum(temp1);sum(temp2)];
 % recalculate the Optimal Wiener weights with bias term
  W2(:,n) = inv(R)*P;
end

figure(1);clf;plot(f,abs(W1(1,:)-W2(1,:))*100/A,'ko',f,abs(W1(2,:)-W2(2,:))*100/B,'k+')
title('Structural response correlation bias in the optimal weights');
ylabel('% bias error');xlabel('Excitation bandwidth (Hz)');
legend('Weight 1','Weight 2');
```

VITA

Christopher Fannin was born May 19, 1972 in Washington, D.C. and grew up in Fairfax County, Virginia. He graduated from Thomas Jefferson High School for Science and Technology in June, 1990. In the fall of 1990, he started his undergraduate work in Mechanical Engineering at Virginia Tech. During his undergraduate program, Chris was a co-op for five semesters with B&W Nuclear Technologies (now Framatome Technologies) in Lynchburg, VA. He worked one semester in stress analysis and four semesters as a tooling designer. His last co-op term was the summer of 1994 which he spent as an intern exchange with Framatome in Chalons-sur-Saone, France. He received his Bachelor of Science, Magna Cum Laude in May, 1995. He started his Master's work in Structural Dynamics and Controls in the summer of 1995. He was a GTA for the department for a year and a half and enjoys the dynamics and stimulation of teaching. In his last semester, he served as a lead TA, which involved the additional responsibilities of overseeing the successful operation of the labs and administration of the course. In January, 1997, he began his Ph.D. research in active combustion control, where he will be using neural networks for modeling and control of thermoacoustic instabilities in gas turbine combustors.